INFORMATION TO USERS

This manuscript has been reproduced from the microfilm master. UMI films the text directly from the original or copy submitted. Thus, some thesis and dissertation copies are in typewriter face, while others may be from any type of computer printer.

The quality of this reproduction is dependent upon the quality of the copy submitted. Broken or indistinct print, colored or poor quality illustrations and photographs, print bleedthrough, substandard margins, and improper alignment can adversely affect reproduction.

In the unlikely event that the author did not send UMI a complete manuscript and there are missing pages, these will be noted. Also, if unauthorized copyright material had to be removed, a note will indicate the deletion.

Oversize materials (e.g., maps, drawings, charts) are reproduced by sectioning the original, beginning at the upper left-hand corner and continuing from left to right in equal sections with small overlaps.

Photographs included in the original manuscript have been reproduced xerographically in this copy. Higher quality 6" x 9" black and white photographic prints are available for any photographs or illustrations appearing in this copy for an additional charge. Contact UMI directly to order.

Bell & Howell Information and Learning
300 North Zeeb Road, Ann Arbor, MI 48106-1346 USA
800-521-0600

Anomalous Magnetic Phase Transitions in the Quasi-One-Dimensional Systems NaV_2O_5 and Cu_3WO_6 Detected by Muon Spin Relaxation

Yasunori Fudamoto

Submitted in Partial Fulfillment of the
Requirement for the Degree
of Doctor of Philosophy
in the Graduate School of Arts and Sciences

Columbia University

2000

Abstract

Anomalous Magnetic Phase Transitions
in the Quasi-One-Dimensional Systems NaV_2O_5 and Cu_3WO_6
Detected by Muon Spin Relaxation

Yasunori Fudamoto

Static spin freezing at $T \sim 11$ K was detected by muon spin relaxation (μSR) in NaV_2O_5, which is widely considered to have a spin-singlet state below 35 K. This spin freezing is suppressed in charge-doped Na deficit samples $Na_xV_2O_5$ with $x = 0.99$ and 0.90, in which spin gap formation is also suppressed. We discuss a few different scenarios to interpret this spin freezing.

Static spin freezing, with a very small average ordered moment, is also observed at $T = 7.0$ K in μSR measurements of polycrystalline Cu_3WO_6, in contrast to the previous neutron scattering and susceptibility studies in which a spin gap was observed. Zn-doped $Cu_{3-x}Zn_xWO_6$ with $x > 0$, however, exhibit no signature of spin freezing. The μSR results of $Cu_{3-x}Zn_xWO_6$ are similar to those of a charge-ordered system $Na_xV_2O_5$.

Contents

Acknowledgements

I would like to express special thanks to Professor Yasutomo J. Uemura at Department of Physics, Columbia University, for providing me an opportunity to work in his μSR group and to work on research topics of prime current interest. It was very scientifically stimulating and educationally beneficial to learn on various research topics in solid state physics studied by his group. His generous financial support enabled me to participate in our collaborators' experiments and several academic conferences, which enriched my academic life in the graduate school.

I would like to thank Professor Graeme M. Luke at Department of Physics and Astronomy, McMaster University, for his supports, especially for making our beamtime efficient by his experimental techniques. He has done early stage of the study of vanadium oxides presented in this thesis, and later allowed me to share the benefit of the new findings. I am also grateful for his proofreading papers and proposals I have written in the past three years.

The measurements and the data analysis were performed with my comrades at Department of Physics, Columbia University; a postdoctoral fellow Kenji M. Kojima, graduate students Ben Nachumi, Mike Larkin, Ioana M. Gat, and Andrei Savici, an undergraduate student Jack Merrin, and a visiting scientist Toshimitsu Ito. Working with them was both entertaining and educational.

I am very grateful to Professor Yutaka Ueda and Doctor Masahiko Isobe at the Institute for Solid State Physics, the University of Tokyo, for providing the specimens of vanadium oxides including $Na_xV_2O_5$.

I would like to express sincere thanks to Professor Kunimitsu Uchinokura, Doctor Masashi Hase, Mr. Naoki Koide, and Mr. Takatsugu Masuda at Department of Applied Physics, the University of Tokyo, for providing the specimens of $Cu_{3-x}Zn_xWO_6$.

Professor Douglas E. MacLaughlin at Department of Physics, University of California. Riverside and Doctor Robert H. Heffner at Los Alamos National Laboratory allowed me to join their μSR experiments of UCu_4Pd and $PrInAg_2$, and to become a coauthor of their papers.

The μSR experiments necessarily involved the efforts of a relatively large group of people at TRIUMF. I would like to thank especially Doctors Syd Kreitzman, Bassam Hitti, Curtis Ballard, and Mel Good.

Doctor Hikomitsu Kikuchi at Department of Physics, University of Tsukuba, taught me how to produce the ceramic specimens of $Zn_xCr_{2x}Ga_{2-2x}O_4$, NaV_2O_5, and and Cu_3WO_6.

Professor Shin-ichi Uchida and Doctor Hiroshi Eisaki at Department of Advanced Materials Science, the University of Tokyo, gave me the opportunity to learn the crystal growths of $Sr_{14-x}Ca_xCu_{24}O_{41}$ and $LaCuO_{2.5}$.

I acquired the basics in science at Lehman College and Hunter College of the City University of New York. It was very fortunate to have my undergraduate education there.

Finally, I thank my family, Tomoe and Mitsuhiro Fudamoto, and Itsuko and Katsuhiko Nitta for their unlimited encouragement and forgiveness, without which my graduate study would not be successful.

This work was supported financially by the New Energy and Industrial Technology Development Organization, Japan, and the National Science

Foundation. USA.

Chapter 1

Introduction

Study of the magnetic properties of low-dimensional systems is a central research area in modern magnetism. Low dimensionality suppresses formation of long range order; there is no long-range order in any purely one-dimensional systems. Even in actual systems where a finite three-dimensional coupling often helps the formation of long-range order, the ordering temperature is much reduced from the energy scale of exchange interaction, and the ordered moment size is also strongly reduced. Thus, the predominant spin degrees of freedom remain in the dynamic spectral weight even at $k_B T << J$.

Alternatively, quasi-one-dimensional spin systems often end up in non-magnetic singlet ground state via the formation of a spin gap (Fig. 1.1). Such systems include a spin-Peierls system (Fig. 1.2) $CuGeO_3$ [1], a two-leg spin ladder $SrCu_2O_3$ [2], and a Haldane system (Fig. 1.3) Y_2BaNiO_5 [3]. Contrary to the robustness expected from the high energy scales of the spin gap, the non-magnetic ground states of these systems can easily be altered to magnetic order by a very small amount (as low as 0.1 at.%) of (Cu,Zn) substitution [4, 5] or charge doping [6]. With substantial charge doping, some spin gap systems exhibit superconductivity [7].

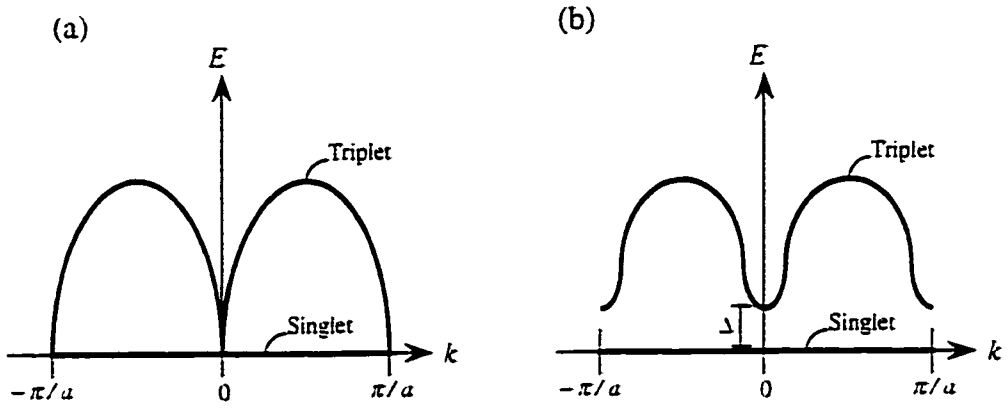

Figure 1.1: (a) Spin-wave spectrum of the antiferromagnetic linear chain (Des Cloizeaux-Pearson mode [8]). There is no energy gap in singlet-triplet excitations. (b) In real systems, however, singlet ground state is often stabilized energetically by the formation of a spin gap Δ.

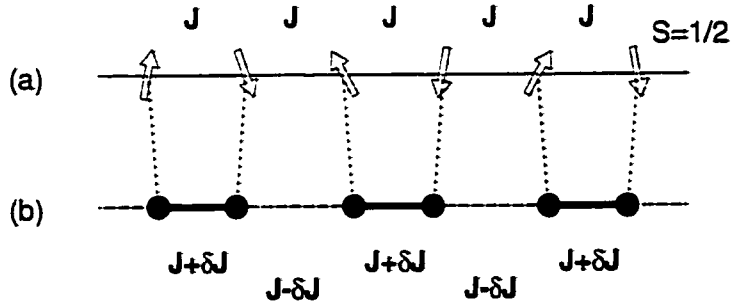

Figure 1.2: A spin-Peierls state: (a) An $S = 1/2$ spin chain with an uniform antiferromagnetic interaction J. (b) The lattice-dimerized state below the spin-Peierls transition temperature T_{SP}.

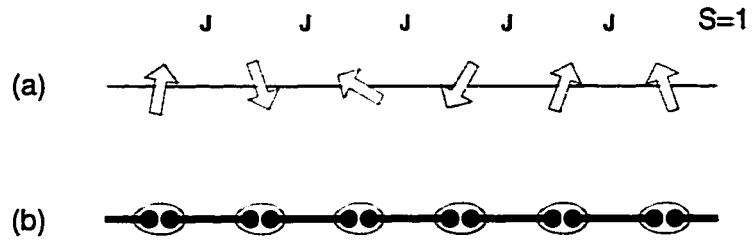

Figure 1.3: The formation of a Haldane gap: (a) An $S = 1$ spin chain. (b) The schematic view of the Valence Bond Solid state, which is based on many singlet pairs. The circle at each site represents the projection of two $S = 1/2$ spins to one $S = 1$.

Recently quasi-two-dimensional antiferromagnets have also attracted special interest as a parent compound of high-T_c superconductors. At low doping the cuprates exhibit long-range antiferromagnetic order, followed by the appearances of metallic conductivity and superconductivity at higher doping. The existence of a pseudo-gap seems to be closely related to the appearance of high-T_c superconductivity, since the pseudo-gap and the T_c curves in the phase diagram merge at the optimum doping, at which T_c becomes the highest (Fig. 1.4).

Muon spin relaxation (μSR) is a powerful and unique magnetic probe to study low-dimensional spin systems. Freezing of very small and/or random magnetic moment can easily be observed in zero-field μSR. One can also obtain limited but useful information on size and homogeneity of frozen moments. Dynamic spin fluctuations can also be detected, in a rather large time window of fluctuation rates ν ranging between $10^7 \sim 10^{12}$ s^{-1}, via $1/T_1$ measurements in zero and longitudinal fields.

In the present thesis, the study of low-dimensional magnetic systems in

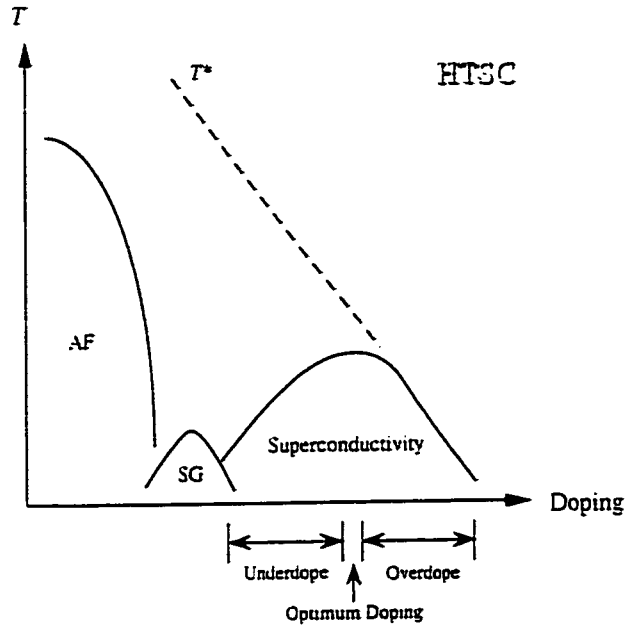

Figure 1.4: Phase diagram of high-T_c superconductors. T^* represents the temperature at which a pseudo-gap is formed.

vanadium oxides and copper oxides will be presented, utilizing the muon spin relaxation technique. Vanadium oxides offer a series of related compounds and enable us to study a variety of magnetic systems. Copper oxides are important as a parent compound of high-T_c superconductors and as a stage for low-dimensional spin systems. Characterizations of low-dimensional systems in vanadates and cuprates would thus contribute to a better understanding of a wide range of novel phenomena.

Chapter 2

Muon Spin Relaxation Technique

The muon spin relaxation (μSR) method is the main magnetic probe used for the present study. In this chapter, theoretical and experimental features of the μSR method will be introduced.

2.1 Stochastic Theories of Spin Relaxation

The spin relaxation function $G_z(t)$ for Gaussian and Lorentzian field distributions will be formulated. One benefit to the μSR method is that measurements in *zero* magnetic field are possible. This condition yields the highest sensitivity to small internal magnetic fields. The theories developed for ordinary spin resonance experiments, such as the Nuclear Magnetic Resonance (NMR) method, often assume the existence of an external magnetic field, and treat internal fields produced by interacting spins with their environments as relatively weak perturbations. This section introduces spin relaxation theories which are applicable to zero-field and low-field conditions. Theoretical spin relaxation function $G_z(t)$ will be compared with experimen-

tal asymmetry $A(t)$ in data analysis.

2.1.1 Larmor Precession

The time evolution of any physical observable A is obtained by solving the Heisenberg equation of motion:

$$\frac{dA}{dt} = \frac{i}{\hbar}[\mathcal{H}, A], \tag{2.1}$$

where [.] represents an anticommutation relation, and $\mathcal{H}$ is the Hamiltonian of the system. Suppose a muon spin $\mathbf{S}$ is placed in a field of $\mathbf{H}$. Then the Hamiltonian is given by $\mathcal{H} = -\gamma_\mu \hbar \mathbf{H} \cdot \mathbf{S}$, where γ_μ is the gyromagnetic ratio of the muon spin ($= 2\pi \times$ 13.554 kHz/G). Thus, the equations of motion for the muon spin $\mathbf{S}$ is:

$$\frac{d\mathbf{S}}{dt} = \frac{i}{\hbar}[-\gamma_\mu \hbar \mathbf{H} \cdot \mathbf{S}, \mathbf{S}]. \tag{2.2}$$

Using identities $[S_i, S_j] = i\varepsilon_{ijk} S_k$, Eq 2.2 becomes:

$$\frac{d\mathbf{S}}{dt} = \gamma_\mu [\mathbf{S} \times \mathbf{H}]. \tag{2.3}$$

We now assume the muon spin $\mathbf{S}$ is initially in the z-axis direction and the field $\mathbf{H}$ makes the polar angle (θ, ϕ) with respect to the z-axis (Fig 2.1), then the z-component of the muon spin polarization $\sigma_z(t) = S_z(t)/S$ at a time t can be obtained by solving Eq 2.3 with above initial conditions:

$$\sigma_z(t) = \sin^2\theta + \cos^2\theta \ \cos(\gamma_\mu H t). \tag{2.4}$$

The spin relaxation function G_z(t)is the ensemble average of the z-component of the muon spin polarization $\sigma_z(t)$ over the field space:

$$G_z(t) = \int d\mathbf{H}^3 \ \rho(\mathbf{H}) \ \sigma_z(t). \tag{2.5}$$

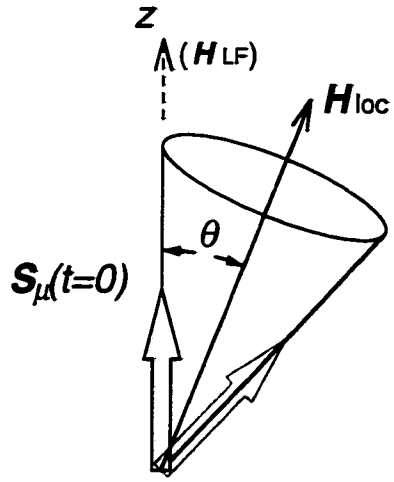

Figure 2.1: Time evolution of the muon spin **S** in the field **H** is given by Eq. 2.4.

If the field distribution $\rho(\mathbf{H})$ is isotropic (or the specimen is polycrystal), then the integration can be done immediately over the angles θ and ϕ yielding:

$$G_z(t) = \int_0^{2\pi}\int_0^{\pi}\int_0^{\infty} H^2 \sin\theta \; dH \; d\theta \; d\phi \; \rho(\mathbf{H}) \; [\sin^2\theta + \cos^2\theta \; \cos(\gamma_\mu H t)]$$

$$= \frac{1}{3} + \frac{2}{3}\int_0^{\infty} \rho(H) \; \cos(\gamma_\mu H t) \; dH, \qquad (2.6)$$

where $\rho(H) = 4\pi H^2 \; \rho(\mathbf{H})$ is the probability distribution of the field magnitude. The first term (*1/3-component*) originates from the fraction of the local field which is parallel to the initial muon spin polarization. This term is an important signature of static relaxation, because its existence doesn't depend on the shape of the field distribution. The second term (*2/3-component*) is the Fourier transform of the field distribution, and hence, contains all information about $\rho(H)$.

2.1.2 Spin Relaxation in Gaussian Field Distribution; the Kubo-Toyabe Theory

The Kubo-Toyabe Function

Suppose magnetic moments are randomly oriented in a condensed phase. Then the probability distribution of a local field, which is a resultant of a large number of elementary contributions from the dipoles, at some point in the lattice is given by the Gaussian [9]:

$$\rho(\mathbf{H}) = \left(\frac{\gamma_\mu}{\sqrt{2\pi}\Delta}\right)^3 \exp\left(-\frac{\gamma_\mu^2 \mathbf{H}^2}{2\Delta^2}\right). \tag{2.7}$$

This is a consequence of the central limit theorem. Since the multiple of the Gaussian distributions is also a Gaussian, the distribution of a field component is given by:

$$\rho(H_i) = \frac{\gamma_\mu}{\sqrt{2\pi}\Delta} \exp\left(-\frac{\gamma_\mu^2 H_i^2}{2\Delta^2}\right), \ (i = x, y, z). \tag{2.8}$$

Substituting Eqs. 2.7 and 2.4 into Eq. 2.5 and integrating, we obtain:

$$\begin{aligned} G_z^{GKT}(\Delta, t) &= \int_0^{2\pi}\int_0^{\pi}\int_0^{\infty} H^2 \sin\theta \; dH \; d\theta \; d\phi \left(\frac{\gamma_\mu}{\sqrt{2\pi}\Delta}\right)^3 \exp\left(-\frac{\gamma_\mu^2 H^2}{2\Delta^2}\right) \\ &\qquad \times [\sin^2\theta + \cos^2\theta \; \cos(\gamma_\mu H t)] \\ &= \frac{1}{3} + \frac{2}{3}(1 - \Delta^2 t^2)\exp\left(-\frac{\Delta^2 t^2}{2}\right). \end{aligned} \tag{2.9}$$

Eq. 2.9 is called the Kubo-Toyabe function [10].

Experimentally, the Gaussian Kubo-Toyabe behavior of the muon spin relaxation, as well as its longitudinal field dependence, is typically observed in spin glass systems, including substances with nuclear magnetic moments, such as MnSi [11] and copper [12].

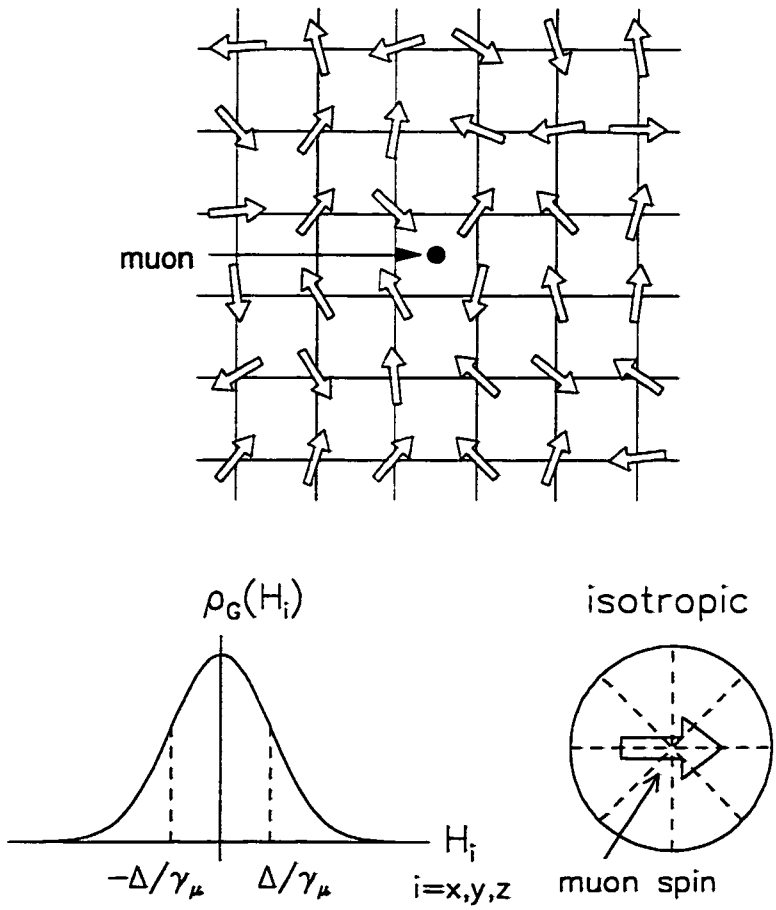

Figure 2.2: Randomly oriented dense spin system. The local field is well approximated with an isotropic Gaussian distribution.

External Longitudinal Field Effect

External field dependence is the characteristic feature of static and quasi-static relaxations. Thus, it is important to investigate the muon spin relaxation in a 'longitudinal field', which is the external magnetic field applied parallel to the initial muon spin polarization ($H_{\rm L}$; see Fig. 2.1). In such a case, the probability distribution of the z-component should be replaced by:

$$\rho(H_z) = \frac{\gamma_\mu}{\sqrt{2\pi}\Delta} \exp\left(-\frac{\gamma_\mu^2 (H_z - H_{\rm L})^2}{2\Delta^2}\right). \tag{2.10}$$

After integrating, the static Gaussian Kubo-Toyabe function in longitudinal fields is expressed as [11]:

$$\begin{aligned} G^{\rm GKT}(\Delta, t; H_{\rm LF}) &= \int d\mathbf{H} \rho_{\rm G}(\mathbf{H} - \hat{\mathbf{z}} H_{\rm LF}) S_\mu(t; \mathbf{H}) \\ &= 1 - 2\left(\frac{\Delta}{\gamma_\mu H_{\rm LF}}\right)^2 (1 - e^{-\Delta^2 t^2/2} \cos \gamma_\mu H_{\rm LF} t) \\ &\quad + 2\left(\frac{\Delta}{\gamma_\mu H_{\rm LF}}\right)^3 \Delta \int_0^t e^{-\Delta^2 \tau^2/2} \sin \gamma_\mu H_{\rm LF} \tau d\tau. \end{aligned} \tag{2.11}$$

In Fig. 2.3, the static Gaussian Kubo-Toyabe function $G^{\rm GKT}(\Delta, t; H_{\rm LF})$ is shown for various longitudinal fields. In zero magnetic field, the function first decays as a Gaussian and then comes back up to the non-relaxing 1/3-component. With a longitudinal field applied, the amplitude of the flat component increases, because the fraction of the field which is parallel to the initial muon spin polarization increases. In static relaxation, the magnitude of the longitudinal field which decouples the relaxation is comparable to the field distribution width ($H_{\rm LF} \sim \Delta/\gamma_\mu$). The distribution width can also be extracted from the Gaussian decay-rate at early times before the recovery.

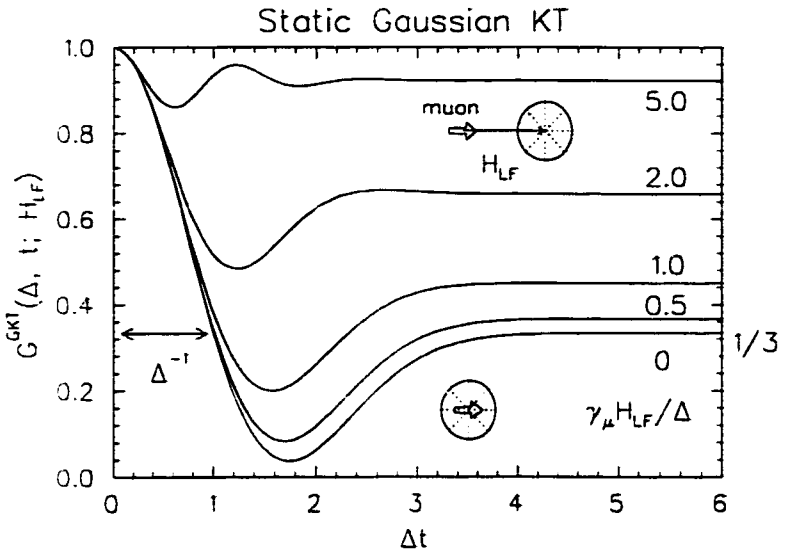

Figure 2.3: The muon spin relaxation in the randomly oriented frozen dense spin system: static Gaussian Kubo-Toyabe function $G^{\mathrm{GKT}}(\Delta t, H_{\mathrm{LF}})$.

Effect of Spin Fluctuations

The effects of field fluctuations have been taken into account with the 'strong collision model' [11, 13]. This model is mathematically simpler than Gaussian-Markoffian model [10, 14] and is useful to obtain qualitative understanding of physics. The strong-collision model assumes that (1) fluctuations occur suddenly, and that (2) every time the local field fluctuates, the muon forgets the previous local field information. Hereafter, the field fluctuation rate (ν) is defined as the Markoffian fluctuation rate, namely, the exponential decay rate of the autocorrelation function of the local fields:

$$\frac{< \mathbf{H}_{\mathrm{loc}}(0) \cdot \mathbf{H}_{\mathrm{loc}}(t) >}{< |\mathbf{H}_{\mathrm{loc}}(0)|^2 >} = \exp(-\nu t), \tag{2.12}$$

where $\tau \equiv 1/\nu$ is the correlation time of the field fluctuation. The strong collision model generally calculates the dynamic muon spin relaxation $G^{\mathrm{D}}(\nu, t)$ from the original static relaxation function $G(t)$ as follows [13]:

$$\begin{aligned} G^{\mathrm{D}}(t) &= e^{-\nu t}G(t) \\ &\quad + e^{-\nu t}\nu \int_0^t dt' G(t-t')G(t') \\ &\quad + e^{-\nu t}\nu^2 \int_0^t dt' \int_0^{t'} dt'' G(t-t')G(t'-t'')G(t'') \\ &\quad + \cdots . \end{aligned} \tag{2.13}$$

The terms of this series account for the muons which experienced $0, 1, 2, \cdots$ field fluctuations in the time interval of $0 \sim t$. The first term $e^{-\nu t}G(t)$ is the static relaxation function $G(t)$ multiplied by the probability $e^{-\nu t}$ that the field does not fluctuate until time t. The second term, which describes the process that the field fluctuate at time t' $(0 < t' < t)$, can be obtained by multiplying $e^{-\nu t'}G(t')$ by $e^{-\nu(t-t')}G(t-t')$, summing over t', divided by the normalization constant $\tau = 1/\nu$. [$G(t')$ is acting as a new initial asymmetry of $G(t-t')$.] The subsequent terms can be derived in the same manner [11].

Fig. 2.4 shows the dynamic Gaussian Kubo-Toyabe function in zero-field for various fluctuation rates (ν). In the slow fluctuation regime ($\nu/\Delta < \sim 0.1$), the fluctuation induces slow relaxation of the 1/3-component. The asymptotic behavior of this relaxation has been obtained as [11]:

$$G^{\mathrm{D}}(t) \sim 1/3 \exp(-2\nu t/3). \tag{2.14}$$

In the intermediate fluctuation regime ($0.1 \lesssim \nu/\Delta \lesssim 2$), the relaxation has a Gaussian behavior in the beginning, but loses the 1/3-component. Hence, the existence/absence of the 1/3-component is a clue which distinguishes static/dynamic relaxation.

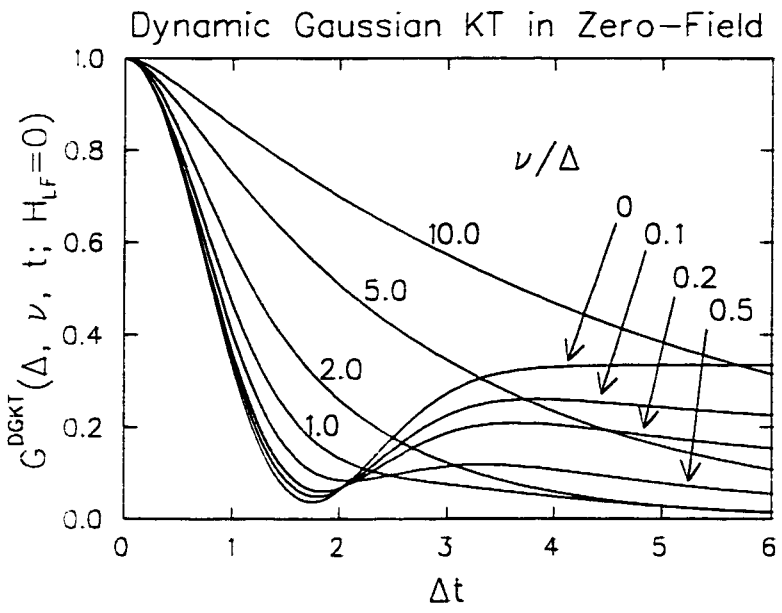

Figure 2.4: The zero-field muon spin relaxation in the fluctuating Gaussian local field [dynamic Gaussian Kubo-Toyabe function $G^{\mathrm{DGKT}}(\Delta, \nu, t; H_{\mathrm{LF}}=0)$].

In the fast fluctuation regime ($\nu/\Delta \gtrsim 10$), the relaxation is approximated by an exponential function [15, 16]:

$$G^{\mathrm{DGKT}}(\Delta, \nu, t; H_{\mathrm{LF}}) \approx \exp(-\lambda t), \tag{2.15}$$

where the relaxation rate is:

$$\lambda = \frac{2\Delta^2 \nu}{\nu^2 + (\gamma_\mu H_{\mathrm{LF}})^2}. \tag{2.16}$$

In this fast fluctuation regime, the relaxation rate (λ) decreases with faster fluctuation rates. This phenomenon is known as the motional narrowing of the T_1-relaxation rate. The longitudinal field dependence of the relaxation rate (λ) is consistent with that of the T_1-relaxation theory [17], which has been developed for nuclear magnetic resonance (NMR).

2.1.3 Spin Relaxation in Lorentzian Field Distribution

Above theories are well applied to other stochastic probability distributions. Here, we treat the Lorentzian field distribution. The Gaussian Kubo-Toyabe theory introduced above is based on Gaussian local field distribution, which is often realized in dense spin systems. In dilute spin systems, such as dilute spin glass alloys, it is known that the dipolar fields from the local moments take a distribution [18]:

$$\rho_{\mathrm{L}}(\mathbf{H}) = \frac{\gamma_\mu^3}{\pi^2} \frac{a}{(a^2 + \gamma_\mu^2 \mathbf{H}^2)^2}, \tag{2.17}$$

where a is the width of the Lorentzian field distribution. This is the three dimensional form of the Lorentzian or Caushy distribution. Eq. 2.17 cannot be decomposed into the distribution of field components, but they are well

approximated as the Lorentzian distributions [19]:

$$\rho_{\rm L}(H_i) = \frac{\gamma_\mu}{\pi}\frac{a}{(a^2+\gamma_\mu^2 H_i^2)}, \ (i = x, y, z). \tag{2.18}$$

The origin of the Lorentzian distribution is considered intuitively as the large variety of the muon sites relative to the local moments (see Fig. 2.5). Since some muons locate relatively far from the local moments (site A of Fig. 2.5), and some close (site B of Fig. 2.5), the local field distribution has a sharper peak around zero (from site A's) and a broader tail (from site B's) than the Gaussian field distribution.

The static muon spin relaxation for the Lorentzian field distribution can be obtained [20] by substituting Eq. 2.17 into Eq. 2.6:

$$\begin{aligned} G^{\rm L}(a,t) &= \frac{1}{3} + \frac{2}{3}\int_0^\infty 4\pi H^2\, \rho_{\rm L}(\mathbf{H})\, \cos(\gamma_\mu H t)\, dH \\ &= \frac{1}{3} + \frac{2}{3}(1-at)\exp(-at) \end{aligned} \tag{2.19}$$

for zero-field.

In the presence of a longitudinal field ($H_{\rm LF}$) the probability distribution of the z-component should be replaced by:

$$\rho_{\rm L}(H_z) = \frac{\gamma_\mu}{\pi}\frac{a}{a^2+\gamma_\mu^2(H_z - H_{\rm L})^2}, \tag{2.20}$$

and the static muon spin relaxation for the Lorentzian field distribution in the longitudinal field is [15]:

$$\begin{aligned} G^{\rm L}(a,t;H_{\rm LF}) &= 1 - \frac{a}{\gamma_\mu H_{\rm LF}} j_1(\gamma_\mu H_{\rm LF} t)\exp(-at) \\ &\quad - \left(\frac{a}{\gamma_\mu H_{\rm LF}}\right)^2 (j_0(\gamma_\mu H_{\rm LF} t)\exp(-at) - 1) \\ &\quad - \left(1 + \left(\frac{a}{\gamma_\mu H_{\rm LF}}\right)^2\right) a\int_0^t j_0(\gamma_\mu H_{\rm LF}\tau)\exp(-a\tau)d\tau, \end{aligned} \tag{2.21}$$

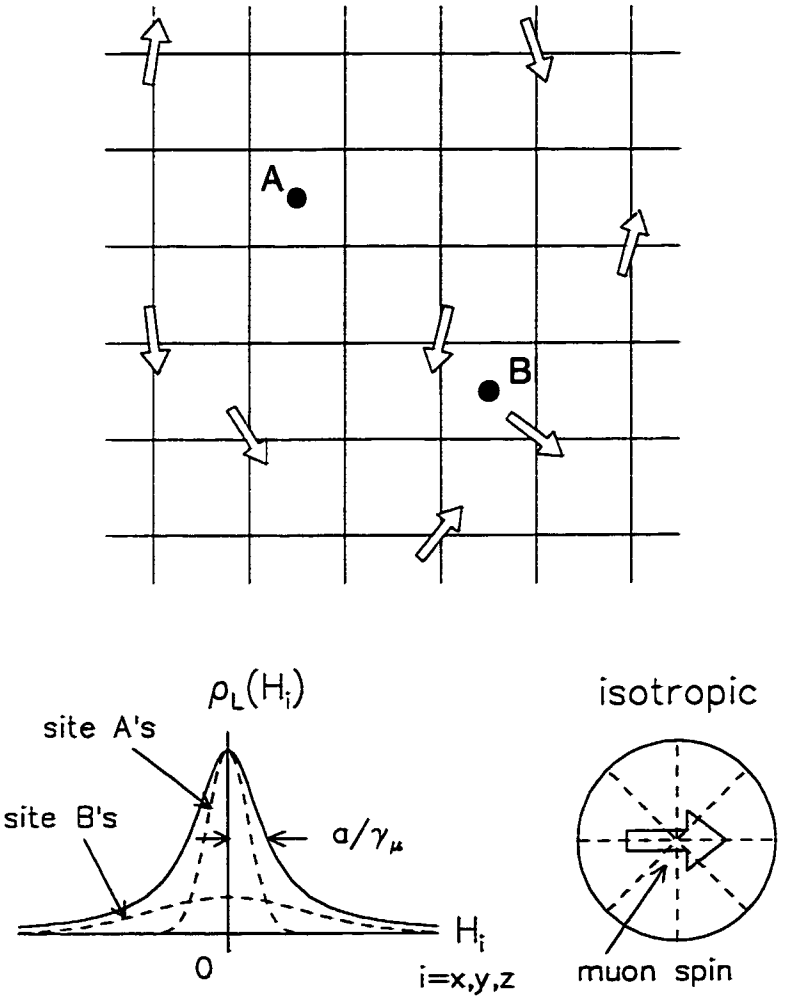

Figure 2.5: A dilute spin system. The local field takes an isotropic Lorentzian distribution.

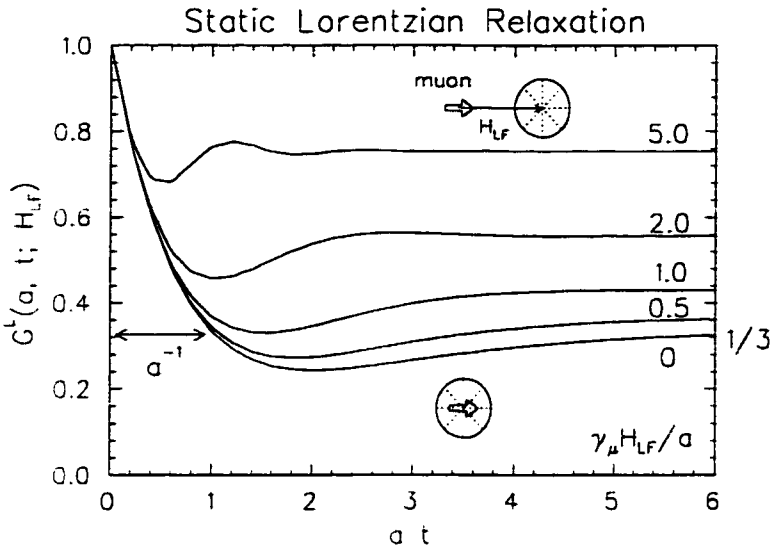

Figure 2.6: The muon spin relaxation in the frozen dilute spin system: static Lorentzian Kubo-Toyabe function $G^{\mathrm{L}}(a, t; H_{\mathrm{LF}})$.

where the $j_i(x)$ are spherical Bessel functions.

In Fig. 2.6, the static Lorentzian relaxation function $G^{\mathrm{L}}(t; a, H_{\mathrm{LF}})$ is shown. In zero-field, the relaxation converges to 1/3 of the full amplitude, which is, again, the signature of static relaxation functions. The 'dip' at $at \sim 2$ is shallower and broader than that of the Gaussian Kubo-Toyabe function (Fig. 2.3), reflecting the broadness of the Lorentzian distribution. The relaxation at early times shows an exponential decay, as the result of Fourier transform of the Lorentzian distribution.

In the presence of field fluctuations, the Lorentzian relaxation function is modulated in a similar manner as the Gaussian Kubo-Toyabe function. Still, one must notice that the Lorentzian distribution results from many *inequivalent* muon sites. A particular muon, which resides at site A (Fig. 2.5),

never experiences the local field at site B during the field fluctuation processes. If one is not aware of this point, and applies the strong collision series (Eq. 2.13) to the static Lorentzian relaxation function $G^{\mathrm{L}}(a,t;H_{\mathrm{LF}})$, one obtains an unphysical result: the absence of motional narrowing [13] in the fast fluctuation regime.

The proper treatment to dynamisize the Lorentzian relaxation function is as follows [15]:

(1) Decompose the Lorentzian field distribution to the sum of many Gaussian distributions, each of which represents the local field distribution at an individual muon site.

(2) Obtain the dynamic *Gaussian* Kubo-Toyabe function for each muon site. This treatment reflects the inequivalence of each muon site for the Lorentzian distribution.

(3) Add each contribution, to restore the Lorentzian field distribution.

This procedure has been formulated [15], using a weighting function $\rho_a(\Delta)$, which is the probability of finding a muon site (Gaussian field width: Δ) in a dilute spin system environment (Lorentzian field width: a). The dynamic Lorentzian relaxation function is obtained:

$$G^{\mathrm{DL}}(a,\nu,t;H_{\mathrm{LF}}) = \int_0^\infty G^{\mathrm{DGKT}}(\Delta,\nu,t;H_{\mathrm{LF}})\rho_a(\Delta)d\Delta, \tag{2.22}$$

where

$$\rho_a(\Delta) = \sqrt{\frac{2}{\pi}}\frac{a}{\Delta^2}\exp\left(-\frac{a^2}{2\Delta^2}\right). \tag{2.23}$$

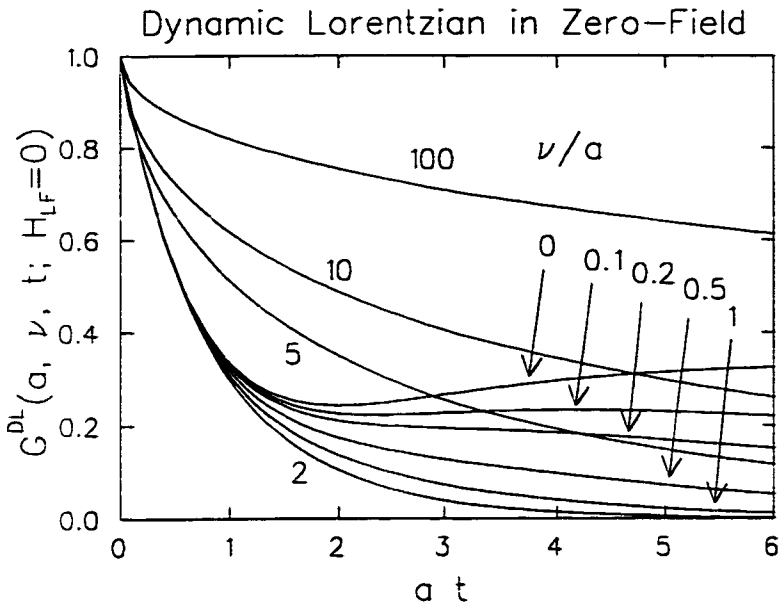

Figure 2.7: The zero-field muon spin relaxation in a fluctuating dilute spin system: dynamic Lorentzian relaxation function $G^{\mathrm{DL}}(a, \nu, t; H_{\mathrm{LF}} = 0)$.

This weighting function, by definition, converts a Gaussian distribution to a Lorentzian distribution:

$$\rho_{\mathrm{L}}(H_i) = \int_0^\infty \rho_{\mathrm{G}}(H_i)\rho_a(\Delta)d\Delta, \ (i = x, y, z). \tag{2.24}$$

In Fig. 2.7, the dynamic Lorentzian relaxation function in zero-field $G^{\mathrm{DL}}(a, \nu, t; H_{\mathrm{LF}} = 0)$ is shown. The effect of the field fluctuations is similar to that of the Gaussian case: in the slow fluctuation regime, the 1/3-component suffers a slow relaxation as [15]:

$$G^{\mathrm{DL}}(a, \nu, t; H_{\mathrm{LF}} = 0) \sim 1/3 \exp(-2\nu t/3), \tag{2.25}$$

and in the fast fluctuation regime, motional narrowing is exhibited. For the Lorentzian distribution, the relaxation in the fast fluctuation regime is

approximated by a square-root exponential function [15]:

$$G^{\mathrm{DL}}(a,\nu,t;H_{\mathrm{LF}}) \approx \exp(-\sqrt{\lambda t}) \tag{2.26}$$

with the relaxation rate:

$$\lambda = \frac{4a^2\nu}{\nu^2 + (\gamma_\mu H_{\mathrm{LF}})^2}. \tag{2.27}$$

Experimentally, the Lorentzian relaxation function, as well as the square-root exponential behavior in the fast fluctuation regime, have been observed in dilute spin glass alloys [15], and the theory has been quite successful in dilute spin systems.

2.2 Experimental Setup

2.2.1 The Basics

The μSR technique is based on the two properties of muons:

(a) muons are 100% spin-polarized, when produced from the $\pi\mu$ decay:

$$\pi^+ \rightarrow \mu^+ + \nu_\mu \tag{2.28}$$

(b) muons decay into one positron and two neutrinos with a lifetime of τ_μ=2.2μs:

$$\mu^+ \rightarrow e^+ + \nu_e + \bar{\nu}_\mu \tag{2.29}$$

The feature (a) results from the 'parity violation' of the weak decays, namely, the fact that only left-handed neutrinos exist. As shown in Fig. 2.8, the muon from the $\pi\mu$ decay has to be spin-polarized, in order to conserve the total spin zero of the pion.

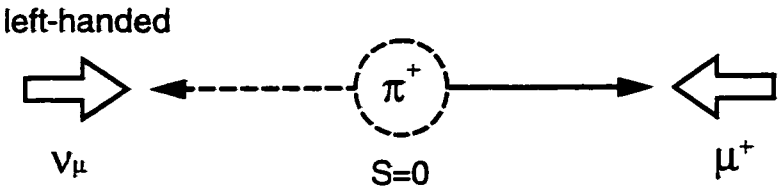

Figure 2.8: Schematic view of the $\pi\mu$ decay. The muon is spin polarized, because pion has spin 0 and neutrino is spin-polarized.

The feature (b) yields an asymmetric angular distribution of the decay-positrons relative to the muon spin direction. The angular distribution of decay positrons depends on their kinetic energy, which ranges from 0 to $E_{\max} \approx m_\mu c^2/2 = 53$ MeV. The angular distribution is expressed as [21]:

$$dN = \frac{1 + a(\epsilon)\cos\theta}{4\pi} d\Omega \times \rho(\epsilon) d\epsilon \tag{2.30}$$

where

$$a(\epsilon) = (2\epsilon - 1)/(3 - 2\epsilon) \tag{2.31}$$

$$\rho(\epsilon) = 2(3 - 2\epsilon)\epsilon^2 \tag{2.32}$$

and $\epsilon = E/E_{\max}$ is the normalized positron energy, θ is the angle of positron emission measured from the muon spin direction, and $d\Omega$ is a small solid angle. After integrating the positron energy, the angular distribution behaves as shown in Fig. 2.9.

The basic idea of the μSR technique follows the next three steps:

(1) a muon is implanted in the sample with its spin polarized.

(2) the muon spin changes its direction because of the magnetic environment around.

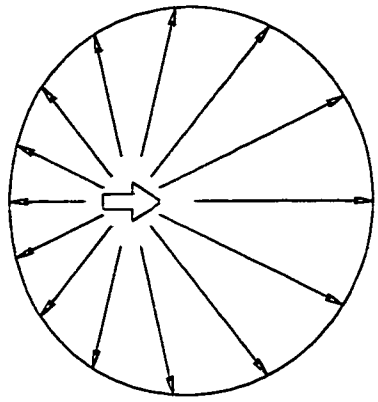

Figure 2.9: Angular distribution of the positron after integrating over its energy. The radial distance represents the relative probability that a positron is emitted in a given direction.

(3) the muon decays into a positron and two neutrinos. The muon spin polarization at the time of the decay is reconstructed by measuring the positron directions for many incident muons.

Detection of Positrons

To reconstruct the muon spin direction, it is convenient to have two positron counters which are placed symmetrically with respect to the sample (muon) position, as shown in Fig. 2.10.

We define the muon spin polarization along the counter axis as $P_\mu(t) = \cos\Theta(t)$, where $\Theta(t)$ is the time evolution of the muon spin angle relative to the counter axis (see Fig. 2.10). The positron count rate of each counter $N_i(t)$ (i=1, 2) is found by integrating the positron angular distribution of this tilted muon spin over the counter solid angle and positron energy. The

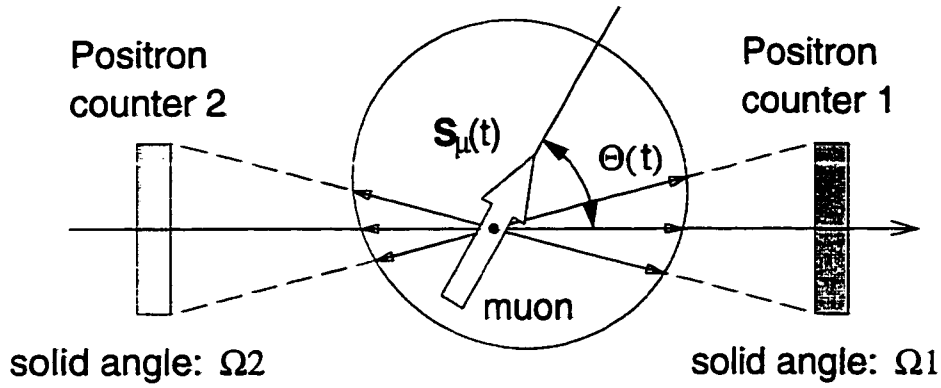

Figure 2.10: A positron counter configuration to reconstruct muon spin polarization.

answer becomes:

$$N_1(t) = N_1^0 \exp(-t/\tau_\mu)(1 + A_1 P_\mu(t)) \quad (2.33)$$

$$N_2(t) = N_2^0 \exp(-t/\tau_\mu)(1 - A_2 P_\mu(t)) \quad (2.34)$$

where

$$N_i^0 = \frac{\Omega_i}{4\pi} \times \int_0^1 \rho(\epsilon)\eta(\epsilon)d\epsilon \quad (2.35)$$

$$A_i = \frac{\int_0^1 a(\epsilon)\rho(\epsilon)\eta(\epsilon)d\epsilon}{\int_0^1 \rho(\epsilon)\eta(\epsilon)d\epsilon} \times \frac{1}{\Omega_i}\int_{\Omega_i} |\cos\theta| d\Omega \quad (2.36)$$

Here, τ_μ ($= 2.2$ μs) is the muon lifetime, $\eta(\epsilon)$ is the detection efficiency of the positron counters and Ω_i is the solid angle of the counter i ($= 1, 2$). A_i is called the asymmetry of the individual counters, which is typically $0.2 \sim 0.3$ in a conventional μSR setup.

The muon spin polarization $P_\mu(t)$, which is the information one would like to obtain from the μSR technique, is calculated by taking the *corrected*

asymmetry (Eq. 2.37), which is essentially the count difference of the two counters normalized by the total count:

$$A_1 P_\mu(t) = \frac{\alpha N_1(t) - N_2(t)}{\alpha\beta N_1(t) + N_2(t)} \tag{2.37}$$

where the parameter $\alpha \equiv N_2^0/N_1^0 = \Omega_2/\Omega_1$ (= 1; ideally) corrects the deviation of the solid angles between the two counters, and $\beta \equiv A_2/A_1$ (= 1: ideally) corrects the difference of the counter asymmetries.

In Fig. 2.11, an example of the positron counts $[N_1(t)]$ and the corrected asymmetry $[A_1 P_\mu(t)]$ is shown. A Larmor precession of the muon spin is seen, as an external magnetic field perpendicular to the initial muon spin direction was applied during this measurement.

The next section presents more details of the experimental setup which is required for the μSR measurements.

2.2.2 Experimental Setup for the μSR Technique

In order to perform μSR measurements, one has to visit a facility which produces many muons. Currently, there are five such 'meson factories' available in the world (see Table 2.1). The heart of these facilities is a particle accelerator which provides a particle beam with a kinetic energy of a few hundred million electron volts (MeV). For this high energy regime, there are two types of accelerators available, namely, the cyclotron and the synchrotron. The time structure of the muon beam reflects the accelerator type of the facility and it determines the details of the μSR setup.

In the synchrotron-based facilities (KEK and RAL), muons come in a pulse, with a spread of $\sim$ 50 ns and a pulse-to-pulse interval of $\sim$ 20 ms. Since the muon arrival time ($t = 0$) is known from the timing signal of the

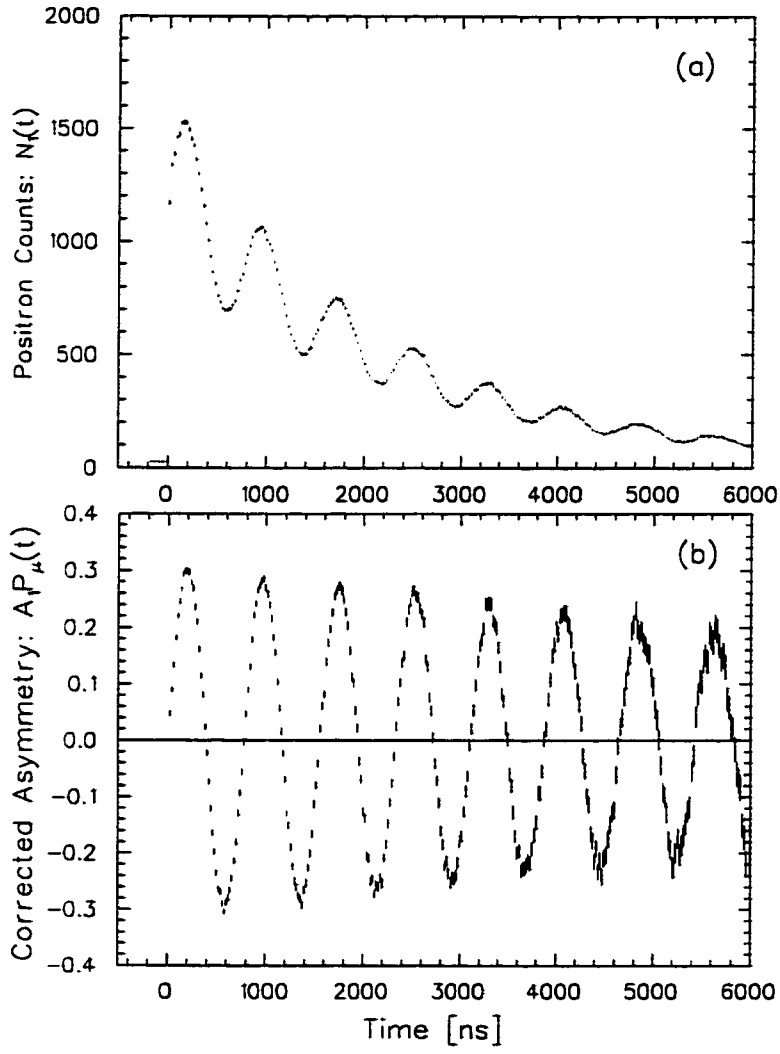

Figure 2.11: (a) A typical time spectrum of one positron counter. (b) The corrected asymmetry (Eq. 2.37) of the same measurement.

synchrotron. μSR measurements are performed by taking the time spectra of decay positrons relative to the muon pulse. The timing resolution of this 'pulse-μSR' method is limited by the muon pulse-width ($\sim$ 50 ns), but the experimental time window is virtually infinite ($\sim$ 20 ms $\gg \tau_\mu = 2.2$ μs). The long experimental time window makes this method convenient for measurements of slow muon spin relaxation. The pulse-μSR method is also convenient to introduce extreme conditions, such as high-magnetic fields [22] and optical radiations [23, 24], using a pulse magnets/lasers synchronized to the muon pulse.

The cyclotron-based facilities (TRIUMF and PSI) provide a continuous muon beam. As a result, one needs a muon counter on the beam path right before the sample, so that one knows a muon arrival time ($t = 0$). The timing resolution of this 'continuous-beam' μSR method is theoretically infinitesimally small; with carefully tuned electronics and small counters, sub-nanosecond resolution ($\Delta t < 1$ ns) may be achieved [25]. The experimental time window is typically $\sim$ 12 μs, which is limited by the random background and the pile-up of second muon arrival.

Since all the data in this thesis were obtained at TRIUMF, more details of the continuous-beam μSR method will be explained below.

Production of a Muon Beam

The heart of TRIUMF (TRI-Universities Meson Facility) is a 520 MeV H^- cyclotron with a high beam-intensity (140 μA). An accelerated proton beam is lead to a production target made of Graphite or Beryllium. Proton hit the target-nuclei and create pions via nuclear reactions.

Table 2.1: Muon facilities in the world

Name (location)	Accelerator	Muons/cm^2/sec (pulse width)
PSI (Switzerland)	cyclotron	$\sim 3 \times 10^6$ (DC)
TRIUMF (Canada)	cyclotron	$\sim 2 \times 10^6$ (DC)
LAMPF (U.S.A)	synchrotron	$\sim 1 \times 10^6$ (0.7ms)
RAL (U.K.)	synchrotron	$\sim 1 \times 10^6$ (100ns)
KEK (Japan)	synchrotron	$\sim 3 \times 10^4$ (50ns)

To obtain muons, one must wait for the pions to decay, which typically takes 26 ns (pion lifetime). To obtain positive muons (μ^+), one can stop positive pions (π^+) in the production target and wait for their decay, because the positive charge of the pions prevent them from being absorbed into the surrounding nuclei. These stopped positive pions produce positive muons which are fully polarized anti-parallel to their momenta (see Fig. 2.8). These muons are called the 'surface muons', because they are emitted from the surface of the production target. Surface muons have (1) high spin-polarization ($\sim$ 100 %), (2) low momentum (29.8 MeV/c $\sim$ 170 mg/cm^2 as the stopping range), and (3) small beam image (a few centimeters in diameter). These features are all favorable for μSR measurements. The muon channels M13, M15 and M20 at TRIUMF are designed to deliver surface muons.

Fig. 2.12 shows a schematic view of the M15 muon channel at TRIUMF. Four dipole magnets (B1-B4) on the beamline bend the beam and select the momentum of the muons. Quadrupole magnets (QAQB, Q1-Q17) focus the muon beam. The DC-separators (SEPARATOR1 and 2) provide crossed electric and magnetic fields perpendicular to the beamline (see the

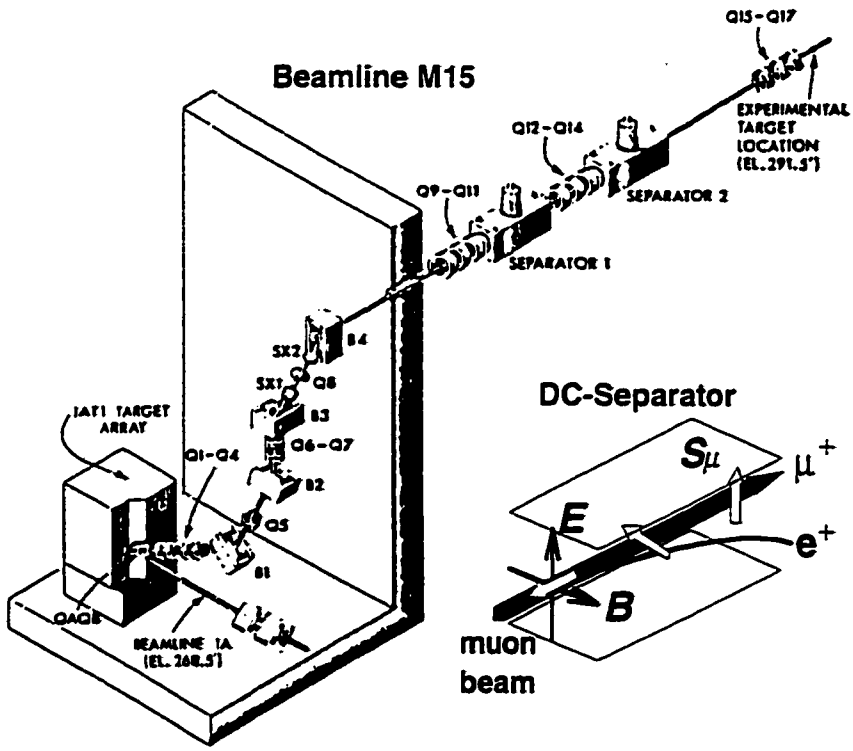

Figure 2.12: A schematic view of the M15 beam line at TRIUMF.

inset of Fig. 2.12). This apparatus eliminates positrons from the muon beam by setting the field ratio (E/B) to the muon velocity (v_μ). Secondly, this apparatus can rotate muon spins away from the momentum direction, by applying higher E and B fields. All of the surface muon channels at TRIUMF are equipped with at least one DC-separator; M20 and M15 have the capability to rotate the muon spins by 90°.

μSR Spectrometer

The muon beam is tightly collimated to the sample size at the end of the beam pipe, which is sealed with a thin Kapton or mylar window. Muons pass through the beam window and reach the spectrometer: a complex of a cryostat, particle counters and magnets. Fig. 2.13 shows a schematic top-view of a typical μSR spectrometer.

Particle Counters

The particle counters used in conventional μSR measurements are usually plastic scintillator (dark gray in Fig. 2.13) attached to a photo-tube (black) through a light-guide; the photo-tube gives an electrical pulse when a charged particle (μ^+ or e^+) passes through the scintillator. The muon counter, which is placed between the beam window and the sample, provides the muon arrival signal ($t = 0$). The scintillator of the muon counter is thin (thickness $\sim$ 0.25 mm) so that it doesn't prevent muons from reaching the sample. The positron counters (Backward, Forward, Left and Right counters) are placed symmetrically with respect to the sample position, so that the muon spin polarization can be reconstructed as described in section 2.2.1. The scintillators for the positron counters are relatively thick ($\sim$ 1 cm) to have a

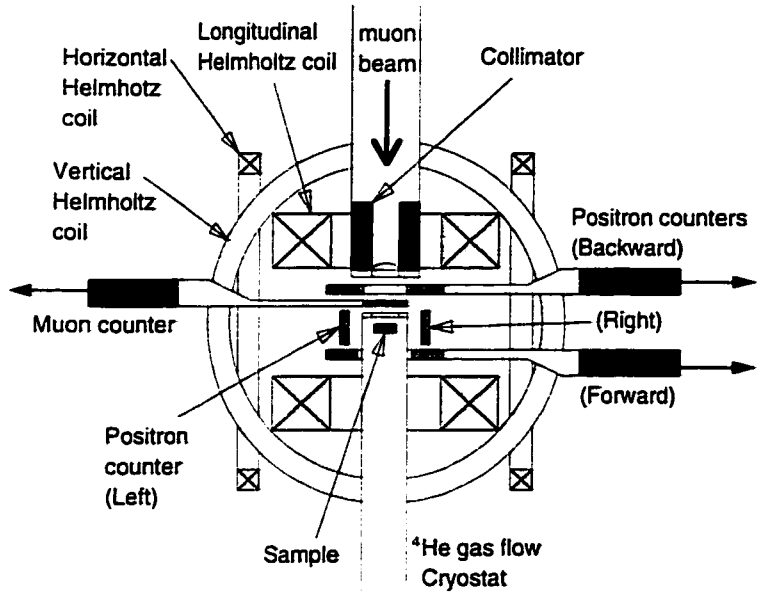

Figure 2.13: A top-view of a typical μSR spectrometer, which is an assembly of particle counters, magnets and a cryostat.

good detection efficiency for the relativistic decay positrons (momentum $\sim$ 50 MeV/c).

Magnets

A μSR spectrometer is usually equipped with three pairs of Helmholtz coils: one longitudinal ($\mathbf{H} \parallel$ beamline), one vertical and one horizontal pair. These three magnets makes it possible to null the magnetic field at the sample position for zero-field (ZF) μSR measurements. The longitudinal magnet is also used to apply higher external magnetic field during the measurements.

Cryostats

For the μSR measurements of this thesis, two types of cryostats were employed: a ^{4}He gas flow cryostat and a dilution refrigerator. In the ^{4}He gas flow cryostat, the samples were suspended close to the end of a sample chamber, which is a tube ($\phi \sim 7.5\,\mathrm{cm} \times L \sim 50\,\mathrm{cm}$) with a sealed beam window at the sample position. The chamber has a ^{4}He-diffuser close to the sample position, which is connected to a ^{4}He dewar through a capillary with a needle valve. The diffuser provided gaseous ^{4}He to the sample chamber. The cooling power was roughly controlled with the needle valve. The other end of the sample chamber is connected to a rotary vacuum pump. By reducing the pressure in the sample chamber, the cryostat can reach $\sim$ 1.8 K. There are two heaters equipped in this cryostat: one at the diffuser, and the other at the sample position. The diffuser heater finely tuned the cooling power, and determined the temperature of the ^{4}He gas flowing to the sample chamber. The sample heater was connected to a temperature controller (Lakeshore DRC-92C) and stabilized the temperature at the sample position.

For temperature reading and control, a carbon glass register and a platinum thermometer (or a GaAlAs diode for the full temperature range) were used at the sample position and at the diffuser.

The dilution refrigerator we used (Oxford 400) is a conventional closed-cycle refrigerator, circulating the ^{3}He/^{4}He mixture. The sample was attached to a sample holder, which was screwed onto the mixing chamber. Since the samples were in vacuum, the cooling power for the sample depends on the thermal conduction. To maximize the thermal conduction, Apiezon grease or GE varnish was applied between the sample and the sample holder. The cooling power was controlled by the circulation rate of the ^{3}He/^{4}He mixture, while the temperature was controlled using a heater on the mixing chamber. The mixing chamber was equipped with a carbon resistor for temperature reading; the base temperature of the refrigerator was typically 20 mK. The dilution refrigerator shares a ^{4}He dewar with a superconducting Helmholtz coil which supplied a field parallel to the beam axis at the sample position.

Table 2.2 summarizes the features of the three spectrometers currently available at TRIUMF. Most of the data presented in this thesis have been obtained using the OMNI and the DR spectrometers, often in combination.

Electronics and Data Handling

The signals from the muon/positron counters are shaped to a logical pulse using the CFD (Constant Fraction Discriminator), which is commonly used in nuclear experiments. The logical pulses are handled by the circuits shown in Fig. 2.14, in order to take the time spectrum of the μe decay. The main scheme of the electronics follows the thick solid lines; the 'muon signal'

Table 2.2: The μSR spectrometers at TRIUMF.

Name	Cryostat (temperature range)	Longitudinal Magnets (H_{max})
DR	Dilution Refrigerator (20 mk~20 K)	Superconducting Helmholtz (60 kG)
OMNI	^{4}He flow cryostat (1.8 K~300 K)	Normal Helmholtz coil (3.5 kG)
HELIOS	^{4}He flow cryostat (3 K~300 K)	Superconducting Solenoid (70 kG)

starts the stopwatch called TDC (Time to Digital Converter) and one of the 'positron signals' stops it. The elapsed time between these two events is stored in the histogram memory, along with the information of which positron counter gave the stop signal. The histogram memory is read by the data-taking VAX-computer typically every 5 minutes.

The circuit is equipped with 'pile-up rejection' logic (thin solid line in Fig. 2.14), which is necessary for μSR measurements using a continuous beam, as at TRIUMF. This circuit rejects situations where more than two muons reside in the apparatus within the experimental time window; in this situation, there is no way of knowing which muon decays to a given positron, and therefore, the data must be thrown away. The gate generator with the dashed lines determines the time range of interest for the measurements ($\sim$ 12 μs). This time range is usually set $\sim$ 500 ns shorter than the time window for the pileup rejection.

Using the electronics described as above, as well as the muon-beam and the spectrometer, one obtains the time spectrum of the μe decay, as shown in Fig. 2.15. There is, however, random background overlapping the spectrum,

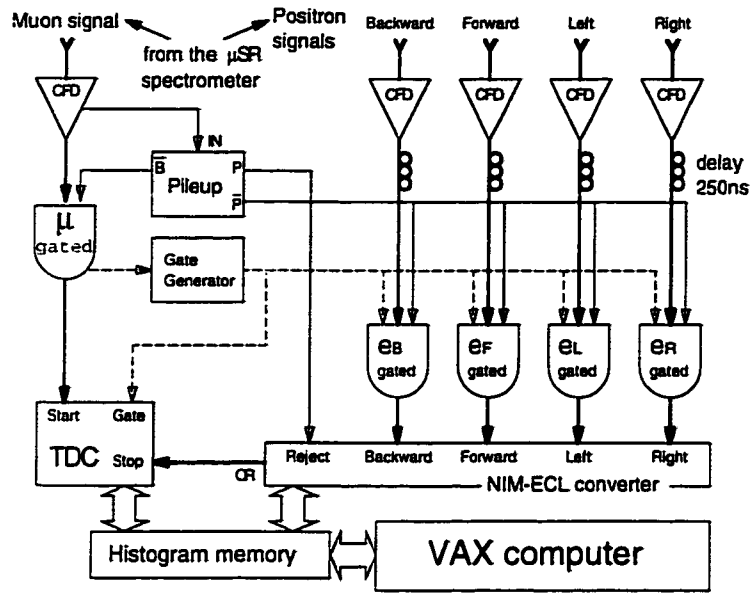

Figure 2.14: A block diagram of the logical circuit for a μSR measurement.

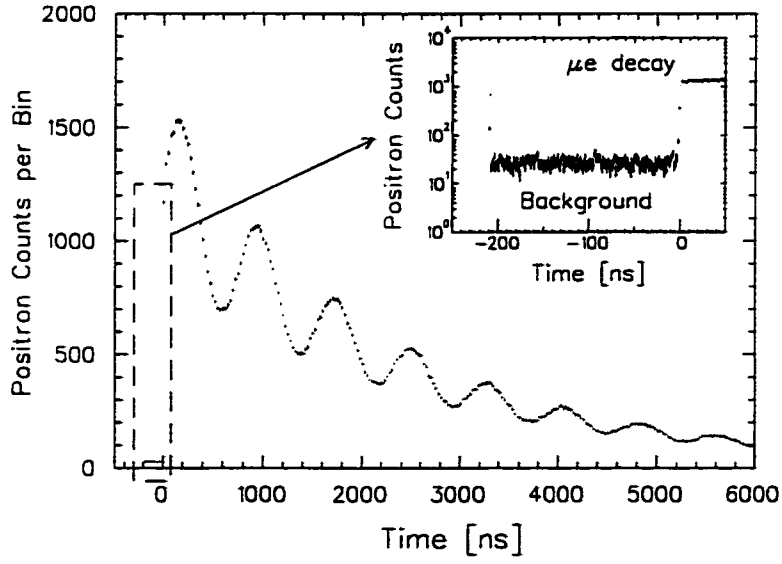

Figure 2.15: A typical time spectrum of one positron counter. The inset shows the same spectrum at the early time range.

an inevitable feature of continuous-beam experiments. Usually, one assumes that the background is time independent, and estimates its level from the spectrum at the $t < 0$ range (the inset of Fig. 2.15). The estimated background is evenly subtracted from the measured spectrum. The existence of the background sets the technical upper-limit of the experimental time range ($\sim$ 12 μs) available for the continuous-beam μSR method.

After subtracting the background, one calculates the corrected asymmetry (Eq. 2.37), and obtains the time evolution of the muon spin polarization, as shown in Fig. 2.11(b).

Counter/Muon Spin Geometries

In general, there are two types of spin relaxation defined: the T_1- and the T_2-relaxation [17]. In μSR measurements, the meaning of these two spin relaxation becomes intuitive, because the muon spin is polarized at $t = 0$.

The T_1-relaxation is defined as the relaxation of the spin component *parallel* to the external magnetic field [17]. In order to measure the T_1-relaxation with μSR, one uses the configuration shown in Fig. 2.16(a), because the muon spin is parallel to the beam axis by default (see Fig. 2.8).

With the same counter configuration [Fig. 2.16(b)], it is also possible to measure T_2-relaxation, which is the relaxation of the spin components *perpendicular* to the external field [17]. In this counter geometry, there is a certain upper limit for the transverse field $H_{\rm TF}$ ($\sim$ 200 G for surface muons), because the muon trajectory curves in the magnetic field, and in the worst case, it misses the sample. For T_2-relaxation measurements in higher fields, the 'Left-Right' (or 'Up-Down') configuration has to be employed [Fig. 2.16(c)].

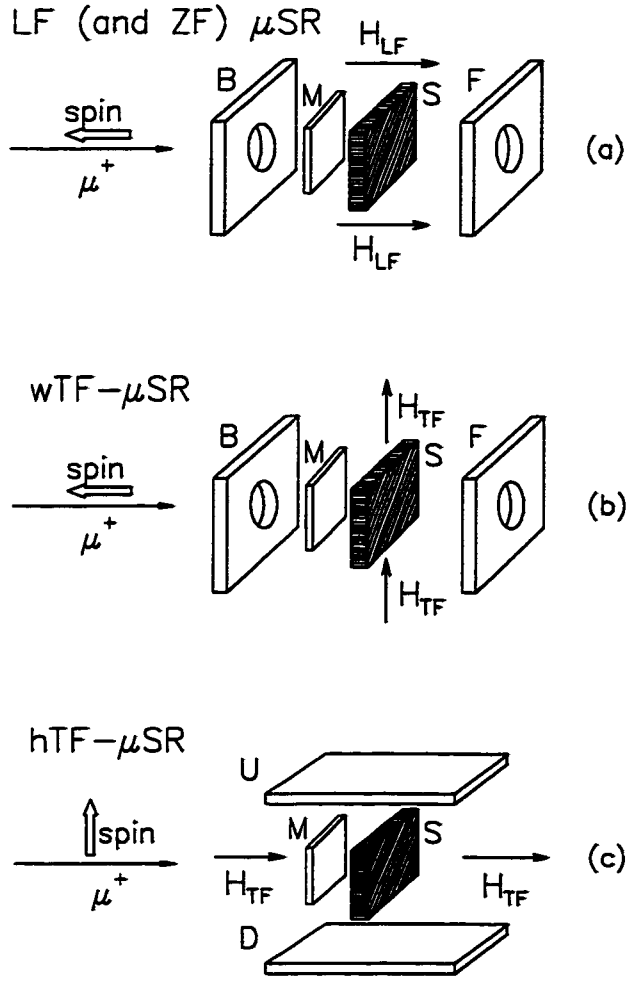

Figure 2.16: (a) Longitudinal field (LF) and Zero field (ZF) μSR. (b) Weak transverse field (wTF) μSR. (c) high transverse field (hTF) μSR.

The measurement with this configuration requires a good DC-separator on the beamline. which is capable of rotating the muon spin perpendicular to the beam (see inset of Fig. 2.12).

Chapter 3

Static Spin Freezing in Charge-Order System NaV_2O_5

We present muon-spin relaxation (μSR) studies of pure ($x = 1.00$) and charge-doped ($x = 0.99$ and 0.90) $Na_xV_2O_5$ systems [26]. We have found static magnetic freezing at $T \sim 11$ K in pure NaV_2O_5, which is widely considered to have a spin-singlet state below 35 K. This spin freezing is suppressed in charge-doped Na deficit charge-doped systems. We present two possible interpretations, unrelated/related to the presence of μ^+, compare their feasibility, and consider a possible relation to recent thermal conductivity results.

3.1 Charge-Order and Singlet Ground State in NaV_2O_5

NaV_2O_5 [27] is the second inorganic compound, after $CuGeO_3$ [1], which has been proposed to show a spin-Peierls transition. Vanadium (V) atoms in NaV_2O_5 have a configuration equivalent to a two-leg ladder structure. Valence counting based on Na^+ and O_5^{10-} indicates that half of the V atoms are in spin-1/2 V^{4+} states while the other half in nonmagnetic V^{5+} states.

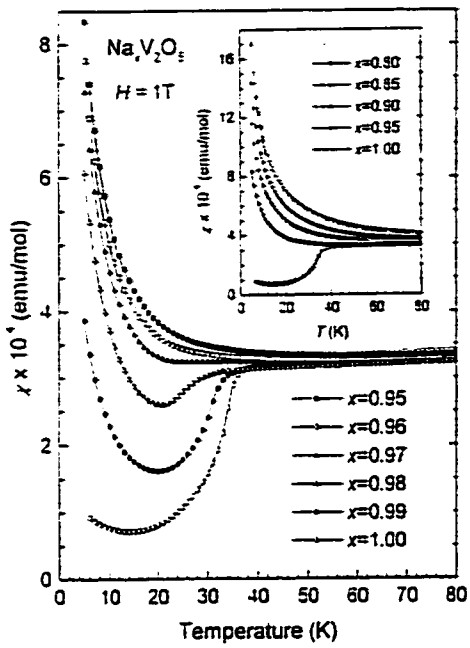

Figure 3.1: Temperature dependence of susceptibility in $Na_xV_2O_5$ [27].

Following the initial discovery of a sharp reduction of the magnetic susceptibility below $T_c = 35$ K [27] (Fig. 3.1), a gap with $E_g \sim 10$ meV was observed in inelastic neutron scattering [28], and a lattice distortion has been detected below T_c by x-ray diffraction [28]. These results were initially interpreted as signatures of a standard spin-Peierls transition. Recently, however, NMR [29] and x-ray [30] measurements found signatures suggesting that the transition is also associated with a charge ordering from a mixed valence $V^{4.5+}$ above T_c to a localization of d-electrons below T_c. The possibility of a zig-zag configuration of the magnetic V^{4+} atoms (Fig. 3.2) has also been discussed theoretically [31]. The zig-zag charge order indeed explains observed discrepancies, such as two excitation branches and an intensity modulation in the inelastic neutron scattering measurement [32, 33], as well as an increase of the lattice constant along the c-axis instead of the b-axis (the ladder direction) in the x-ray diffraction study [28]. While the electronic state below $T_c = 35$ K

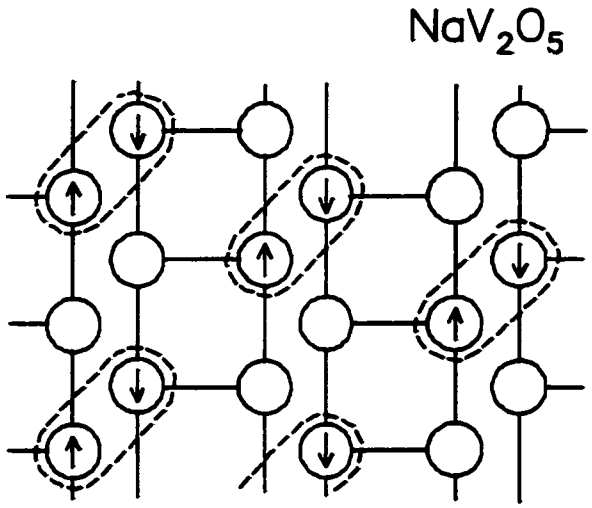

Figure 3.2: Zigzag charge order in $Na_xV_2O_5$ [31].

remains controversial, one-dimensionality in a paramagnetic phase (above T_c) has been confirmed by susceptibility [27] and angle-resolved photoemission [34] studies.

3.2 Static Spin Freezing at 11 K

In Fig. 3.3(a), we show μSR time spectra of the (mosaic) single crystal specimen of NaV_2O_5 [35] at various temperatures in zero external field (ZF). The spectra below $T \sim 11$ K exhibit a fast reduction of the muon-spin polarization followed by a slow depolarization of about 1/3 of the total asymmetry, which is characteristic of relaxation due to co-existing static and dynamic random local fields. Figure 3.3(a) also shows the existence of two different relaxation rates at low temperatures, indicating two magnetically inequivalent muon environments. There is no sign of coherent oscillation of

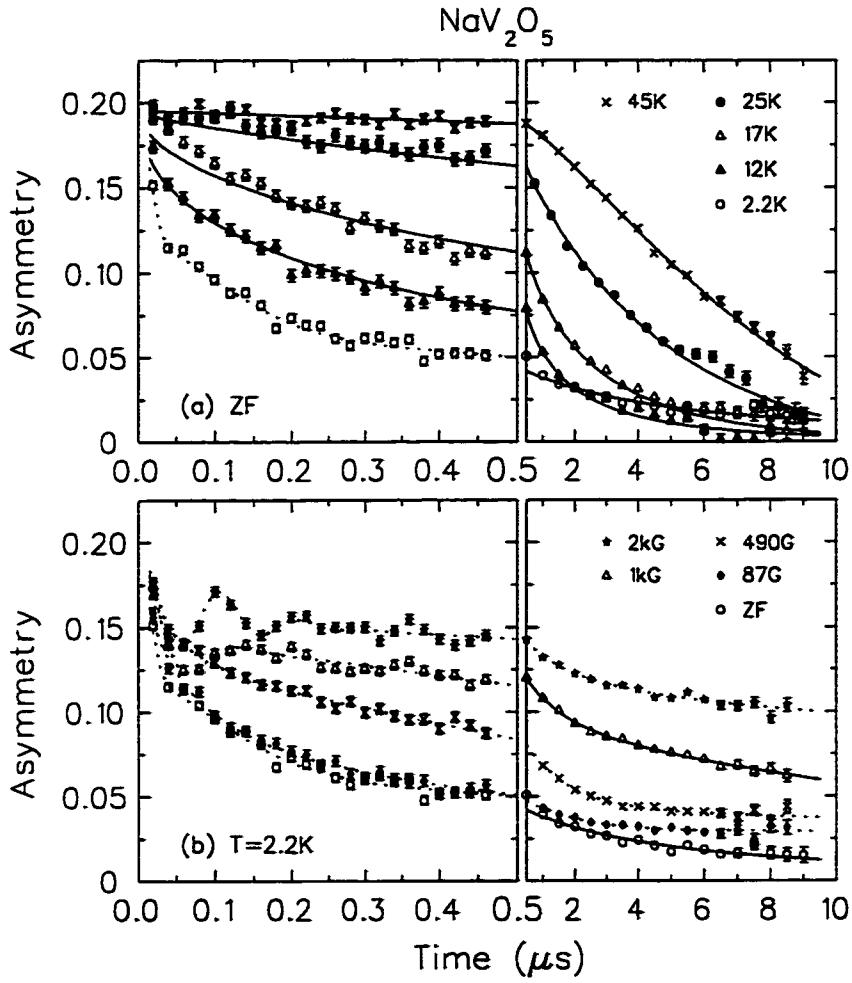

Figure 3.3: μSR spectra in the (mosaic) single crystal specimen of NaV_2O_5 (a) in ZF at several temperatures, and (b) in several LF at 2.2K. Solid lines represent the best fit to Eq. 3.1, while dashed lines are guides to the eye.

the muon spin, indicating broadness of the distribution of the local field. The predominance of static random fields at low temperatures has been confirmed by decoupling the relaxation in longitudinal fields (LF) as shown in Fig. 3.3(b). The magnitude of the static field estimated from this decoupling is about $100 \sim 400$ G. Slow decay in the LF data suggests that dynamic spin fluctuations remain persistent even at $T \to 0$.

The observed spectra at low temperatures, however, do not have a polarization minimum of the damped oscillation of a 2/3 component, which is expected in static ZF relaxation functions for Gaussian and Lorentzian field distributions. This form has also been observed by μSR in other systems, such as $CeCu_{0.2}Ni_{0.8}Sn$ [36] and Zn-doped $SrCu_2O_3$ [37]. Recently, it has been found that such a "dipless" or "shallow-minimum" lineshape could be constructed from models [37, 38] involving spatial decay of moment size. However, it is unclear whether or not these results are directly applicable to the present case.

The local field of $\geq 10^2$ G is much larger than ~ 5 G expected when 1 % of randomly located V^{4+} moments undergo spin freezing, similar to dilute-alloy spin glasses. This feature implies that the observed local field cannot be ascribed to the freezing of dilute impurity moments. (A Curie term in the susceptibility of our specimen corresponds to less than 0.1 % of free $S = 1/2$ moments.) To account for the observed field amplitude, we have to assume the freezing of at least about 10 % of the V^{4+} moments. Such spin freezing behavior in widely accepted spin gap systems has also been detected by μSR in a plaquette spin system CaV_4O_9 [39] and a zig-zag chain system $KCuCl_3$ [40].

At sufficiently long time, the ZF relaxation lineshape for coexisting static and dynamic random local fields can be approximated as $A(t) \sim (A_0/3)G_z^d(t)$, where A_0 is an experimental initial asymmetry, its 1/3 reduction for the polycrystal case could be somewhat varied for single crystals, and $G_z^d(t)$ is a dynamic relaxation function of stretched exponential form:

$$G_z^d(t) = \exp[-(\lambda t)^\beta]. \tag{3.1}$$

A moderate applied LF should have little effect in the dynamic relaxation process. We thus analyzed the ZF and LF data below the freezing temperature $T_f \sim 11$ K using $A(t) = A_0' G_z^d(t)$ for $t \geq 0.5$ μsec. A_0' is left as a free parameter and remains constant around $\sim 0.3A_0$ for ZF and $\sim 0.7A_0$ for H_L = 1 kG. β is fixed at 1/2, which is the observed value at $T \rightarrow T_f$ from above [see Fig. 3.4(b)]. We employ a one-component function for simplicity, instead of a two-component one for the two different muon environments, assuming they are subject to the same dynamic process.

The stretched exponential function Eq. 3.1 is generally expected, above and below the freezing temperature: (1) when $1/T_1 \propto \omega_i^2/\nu$ is not uniform due to a distribution of the instantaneous local field amplitude ω_i and/or the fluctuation rate ν among different muon sites; and/or (2) for a non-Markoffian spin correlation process. The power β has a value 1/2 (1.0) for the case of spatially dilute (dense) spin systems fluctuating with a single rate $\nu \gg \omega_i$ [15]. Recently, $\beta \rightarrow 1/3$ was observed in the paramagnetic phase of $AgMn$ and $AuFe$ spin glasses [41] near the freezing temperature T_f.

Above $T_f \sim 11$ K, we analysed the data by fitting to $A(t) = A_0 G_z^d(t)$ for the entire time range. A_0 is fixed to the initial asymmetry, and β is allowed to vary in a range ≤ 1.0. For the ZF data, Eq. 3.1 was further

multiplied by a slowly damping Gaussian Kubo-Toyabe function (with a constant relaxation rate $\Delta = 0.10\ \mu\text{sec}^{-1}$) to account for the nuclear dipolar fields. These two functions are multiplied since the two relaxation processes are entirely independent.

Figure 3.4 shows temperature dependences of (a) the dynamic relaxation rate λ and (b) the stretching power β in ZF and $H_L = 1$ kG. A sharp peak of λ and a reduction of β are common signatures observed in spin glass systems around the spin freezing temperature. In Fig. 3.4(c) we show an initial damping rate, the inverse of the time at which the asymmetry is reduced to $\sim A_0/4$, as a rough estimate for the fast static relaxation rate. The initial damping rate at low temperatures is also reduced sharply around T_f. Essentially the same results were obtained in the ceramic specimen of NaV_2O_5.

We can estimate the fluctuation rate ν of the fluctuating moments in the paramagnetic phase $T > T_f$ using $\lambda = 1/T_1 \sim a^2/\nu$, where a denotes the amplitude of instantaneous random local fields. Since the stretched exponential function with $\beta \ll 1.0$ has a very sharp reduction at early times, the relaxation rate resulting from the stretched exponential fit with the low β values tend to underestimate an average depolarization rate. To compensate this effect, we calculated $\lambda^* = \ln(2)/[\ln(2)]^{1/\beta} \times \lambda$. Figure 3.5 shows the inverse average depolarization rate $1/\lambda^*$. $1/\lambda^*$ is proportional to the average fluctuation rate ν^* as $\nu^* \sim a^2/\lambda^*$. Comparing with activated behavior:

$$\nu \propto \exp\left(-\frac{E_g}{k_B T}\right), \tag{3.2}$$

we obtain a gap energy $E_g = 72.2$ K, which is roughly comparable to the spin-gap energy $E_g \sim 110$ K obtained in the neutron measurement [28].

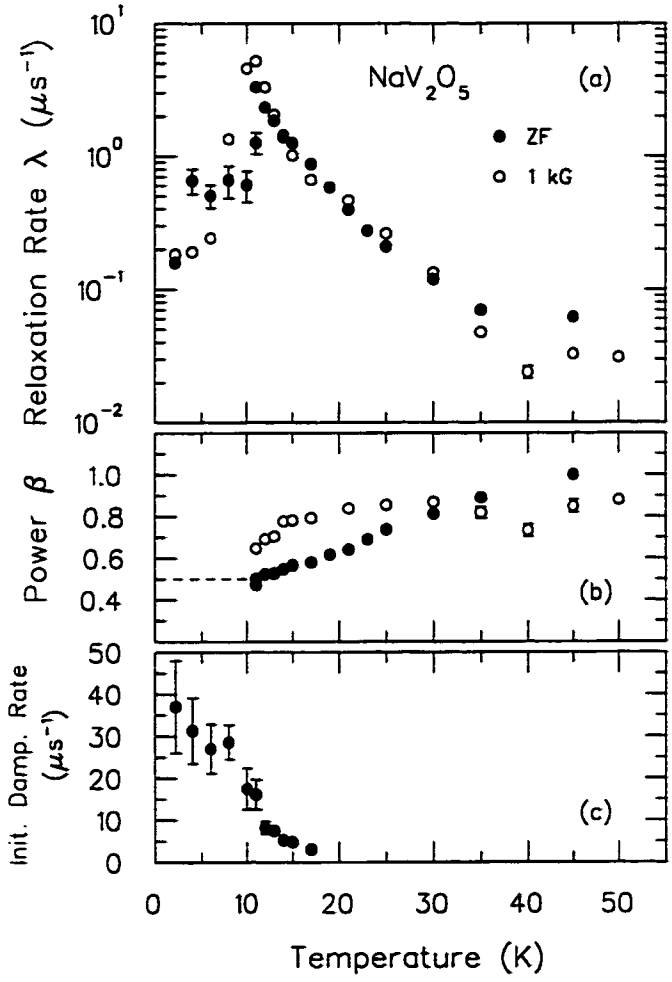

Figure 3.4: Temperature dependence of (a) the dynamic relaxation rate λ, (b) the exponent β defined in Eq. 3.1, and (c) the initial damping rate obtained in NaV_2O_5.

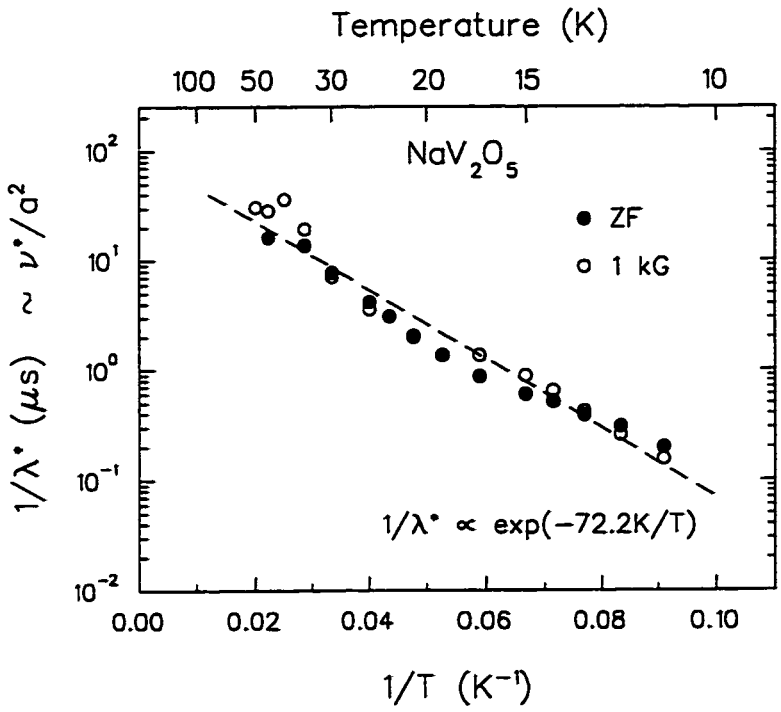

Figure 3.5: Temperature dependence of $1/\lambda^*$ for $T > T_f$, which is proportional to the average fluctuation rate ν^* of the the fluctuating local fields, in NaV_2O_5. The broken line corresponds to thermally activated behavior.

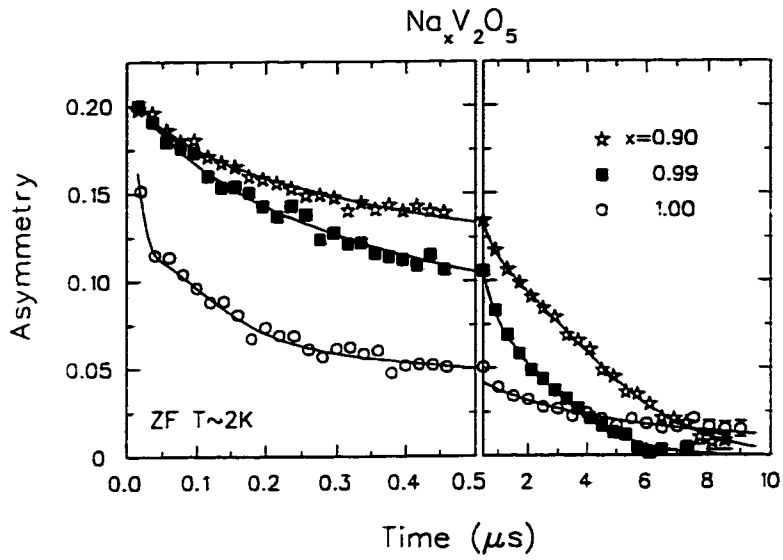

Figure 3.6: ZF-μSR spectra of $Na_xV_2O_5$ (x = 0.90, 0.99 and 1.00) observed at $T \sim 2$ K.

3.3 Suppression of Freezing by Charge Dopings

With a small Na deficiency, NaV_2O_5 can be doped with holes, transforming a fraction of magnetic V^{4+} (spin-1/2) to nonmagnetic V^{5+} (spin-0). The spin-gap formation is suppressed with Na-deficiency, and the reduction of the susceptibility around T_c disappears at $x = 0.97$ [42]. The conductivity was found to increase by more than four orders of magnitude from $x = 1.00$ to 0.90, indicating that the doped holes on a V-O-V chain are mobile and probably move via variable range hopping [42]. Figure 3.6 shows ZF-μSR spectra of $Na_xV_2O_5$ at $T \sim 2$ K. The fast static relaxation observed in pure NaV_2O_5 no longer exists, and the dynamic relaxation rate also becomes much smaller with hole doping. A small Na deficit is thus enough to increase the

fluctuation rate drastically and eliminate the quasi-static component.

3.4 Discussions

Static spin freezing in a spin-gap system, and its suppression with the disappearance of the spin gap, are contrary to naive expectation. In NaV_2O_5, we propose a picture in which a small amount of excess V^{4+} moments, as a subset spin system different from the majority of the V^{4+} moments forming singlet pairs, undergo spin freezing. The singlet coupling of the remaining majority spins may be essential in obtaining an effectively high exchange interaction between the unpaired V^{4+} spins inferred from the rather high transition temperature T_f. This effective exchange coupling would be suppressed with the disappearance of the spin gap, leading to the disappearance of static spin freezing. When the spin gap is suppressed, unpaired spins should be subject to the same fluctuation process as all other majority spins. This would reduce the dynamic muon spin relaxation rate via an exchange narrowing process, similar to a situation in the paramagnetic state above $T_c = 35$ K. The activated behavior of fluctuation rate ν of the unpaired V moments above T_c in Fig. 3.5 can be ascribed to thermal excitations of the neighbouring singlet pairs to magnetically active triplet states.

We should also consider a completely different picture, where the existence of μ^+ perturbs the system, similar to an effect of (Ge, Si) substitutions in $CuGeO_3$, and induces the unpaired spin(s) adjacent to the muon site. Below $T_c = 35$ K, the fluctuation of these muon-induced moments would slow down. When the fluctuation rate ν becomes smaller than a, the internal field may resemble the case of the static spin freezing. We make the following re-

marks concerning this picture: (1) the muon-induced effect does not exist in other spin gap systems $CuGeO_3$ [43], $SrCu_2O_3$ [44], and Y_2BaNiO_5 [6], in which the non-magnetic ground states were confirmed by μSR, or in any known antiferromagnets or spin glass, where μSR detected only those transitions which have corresponding phenomena known in bulk measurements at the same transition temperatures, (2) the slowing down of a single unpaired spin would result in a single exponential time correlation function. This is not consistent either with the observed small power β near T_f, nor with the coexisting dynamic and static fields below T_f. We can not expect persisting dynamic fluctuations at $T \to 0$ for the single spin process, and (3) spin freezing usually occurs in a many-body process which would not be altered by the existence of a local impurity (μ^+).

Recently, Vasil'ev *et al.* [45] found a giant peak in the thermal conductivity κ of NaV_2O_5 around $T \sim 15$K (Fig. 3.7). The height of this peak is sharply reduced with hole doping in Na deficient specimens, and the peak disappears when the spin gap is completely suppressed. Phenomenologically, this behavior may be related to our results, and could possibly give another support for the interpretation of bulk spin freezing. The spin freezing of minority spins below T_f, together with the gap-formation of majority spins, would reduce a magnetic scattering of phonons, and thus helps increase κ. A sharp reduction of κ above T_f can be attributed to increasing spin scattering of the phonons by fluctuations of the minority spins, in addition to thermally activated fluctuations of the majority spins. One should, however, be cautious about this correspondence in view of a much smaller, but somewhat similar peak of κ below the spin Peierls temperature observed even in pure

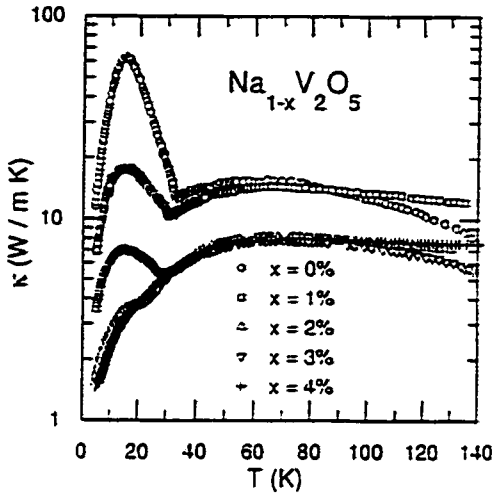

Figure 3.7: Temperature dependence of thermal conductivity in NaV_2O_5 [45].

$CuGeO_3$ [46], a material in which μSR detected no static spin freezing [43].

3.5 μSR Results in Other Vanadates

AV_nO_{2n+1} (A is alkaline metal or alkaline earth) offers a series of related compounds and enables us to study a variety of low-dimensional systems (Table 3.1) including charge-ordered (NaV_2O_5), spin-ladder (CaV_2O_5 and MgV_2O_5), zig-zag chain (LiV_2O_5), dimer (CsV_2O_5), antiferromagnetic long range order (CaV_3O_7 and SrV_3O_7), and 2-D plaquette (CaV_4O_9) systems.

In these Vanadium Oxide compounds, $V^{4+}O_5$ square pyramids are arranged either through edge-sharing or corner-sharing. Thus $S = 1/2$ V^{4+} moments are coupled with two kinds of superexchange interaction via O^{2-} ions, either with (approximately) 90° V-O-V bond or with (approximately) 180° bond. Combination of edge-sharing and corner-sharing arrangements

Table 3.1: A series of related AV_nO_{2n+1} compounds possesses a variety of low dimensional systems.

Compound	Type of System
NaV_2O_5	Charge-Ordered $T_c = 35$ K $\|J\|/k_B = 265$ K $\Delta = 98$ K (NMR) $\Delta = 10$ meV (Neutron Scattering)
CaV_2O_5	2-Leg Ladder $\Delta = 616$ K (NMR)
MgV_2O_5	2-Leg Ladder $\Delta \sim 120$ K (Susceptibility)
LiV_2O_5	Double-Linear/Zig-Zag Chain $\|J\|/k_B = 154$ K
CsV_2O_5	Dimer $\|J\|/k_B = 73$ K
CaV_3O_7	2-D Heisenberg AF $T_N = 23.0$ K
SrV_3O_7	2-D Heisenberg AF $T_N = 34.3$ K
CaV_4O_9	2-D Plaquette (RVB?) $\Delta \sim 100$ K

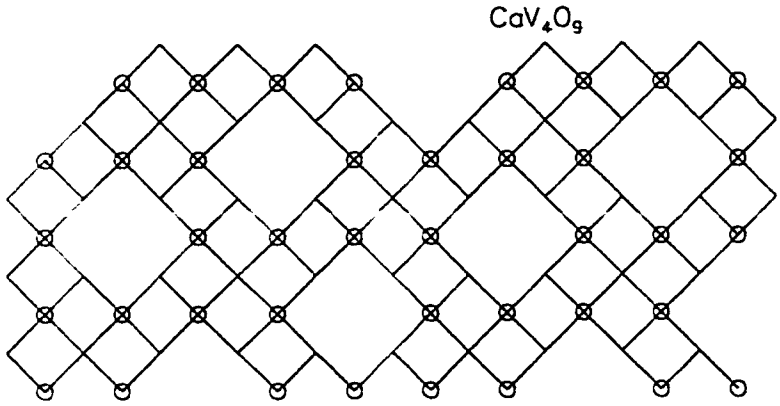

Figure 3.8: Schematic view of V-O plane in CaV_4O_9. Circles indicate V^{4+} ions. while O^{2-} ions are located where lines cross.

generates a variety of crystallographic and hence magnetic structures. We are therefore able to conduct a systematic study of ground states and excitations in series of compounds with the same local structure. Below we summarize μSR studies of these compounds.

2-D Plaquette CaV_4O_9

In CaV_4O_9, the nearest-neighbor V^{4+} ions, connected with the $\sim 90°$ V-O-V (edge-sharing) exchange interaction, form a lattice which may be viewed as four-spin plaquettes (Fig. 3.8). For the next nearest-neighbor coupling of $\sim 180°$ V-O-V (corner-sharing) antiferromagnetic exchange interaction, this lattice can be viewed as inter-penetrating two plaquette lattice, frustrated by the $\sim 90°$ nearest-neighbor coupling. It is not determined yet which exchange interaction (the nearest of the next nearest) is dominant.

A spin gap of $\Delta \sim 100$ K was inferred from susceptibility [47], NMR [48], and neutron [49, 50] measurements. A spin-singlet state with four adjacent

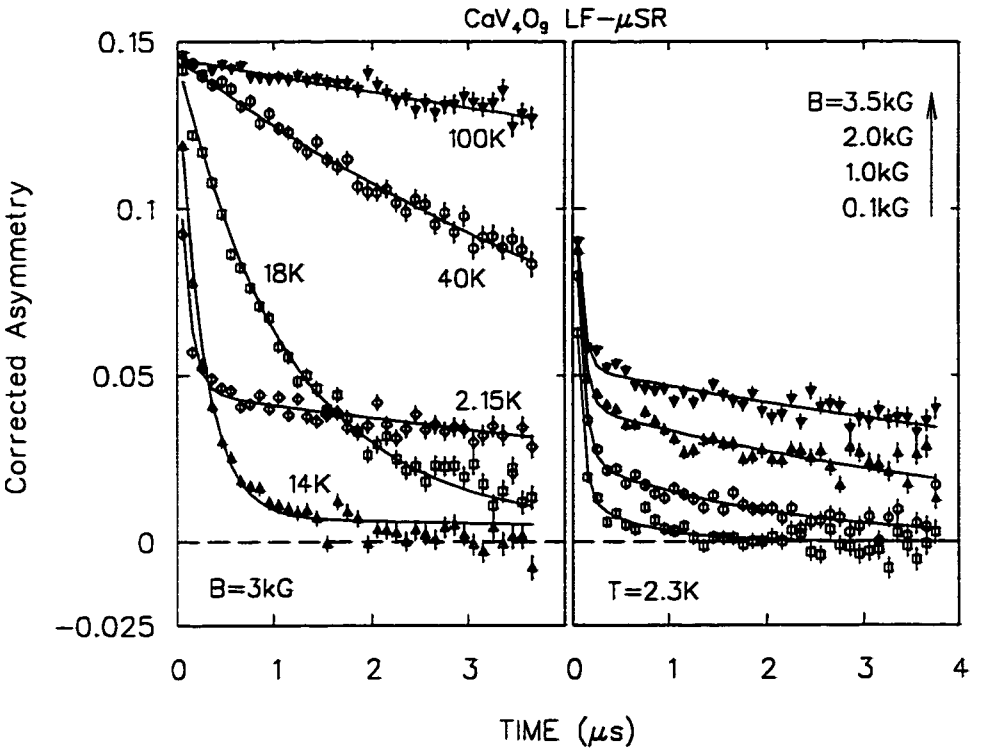

Figure 3.9: (a) Longitudinal-field μSR spectra measured in $H_L = 3$ kG for polycrystalline CaV_4O_9 at $T = 100$ K, 40 K, 18 K, 14 K, and 2.15 K. (b) Longitudinal-field μSR spectra measured at $T = 2.3$ K in polycrystalline CaV_4O_9 for $H_L = 100$ G, 1 kG, 2 kG, and 3 kG.

spins in the resonating valence bond state has been proposed for the plaquette lattice with the antiferromagnetic $\sim 90°$ nearest-neighbor coupling [51, 52], followed by extensive theoretical studies as a possible first example of a spin gap in a quasi-2-D systems [53, 54].

Contrary to the spin-singlet state, which should be expected from the spin gap, we discovered spin freezing in CaV_4O_9, at $T \sim 12$ K [39]. Figure 3.9 shows the zero-field (ZF) and the longitudinal-field (LF) μSR spectra, and Fig. 3.10 shows the muon-spin relaxation rates in these spectra. The

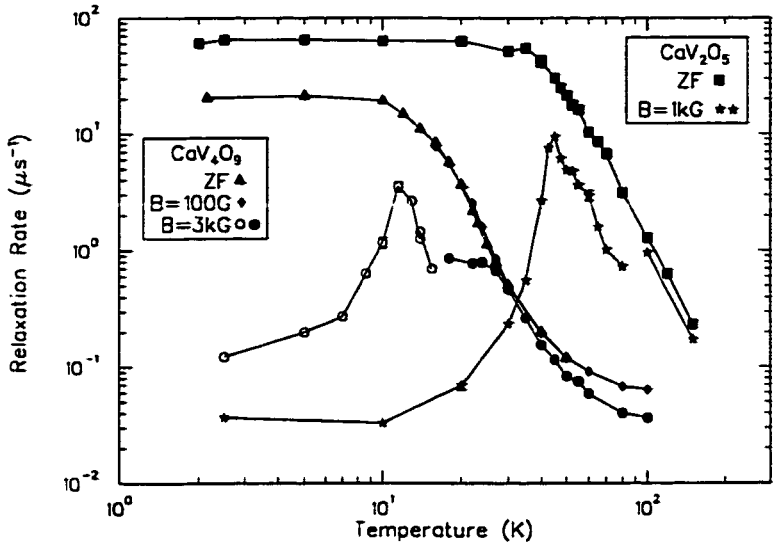

Figure 3.10: Temperature dependence of the relaxation rates in polycrystalline CaV_4O_9 in 100 G (diamonds) and 3 kG (circles) and in polycrystalline CaV_2O_5 in zero-field (squares) and 1 kG (stars).

magnitude of static internal field at low temperatures indicate that majority of V^{4+} moments participate in the spin freezing.

Two-Leg Ladder CaV_2O_5

Theoretical work has shown that antiferromagnetic even-leg ladder systems without inter-ladder interactions possess a spin gap and a singlet ground state [55, 56]. CaV_2O_5 forms a two-leg ladder structure via a corner-sharing interaction J and also inter-ladder zig-zag chain via a edge-sharing interaction J' (Fig. 3.11). Previous susceptibility and pulsed-NMR measurements have been interpreted in terms of a spin-singlet ground state with a spin gap $\Delta \sim 500$ K [57].

In Figs. 3.12 and 3.10, we show the zero-field (ZF) μSR spectra and the

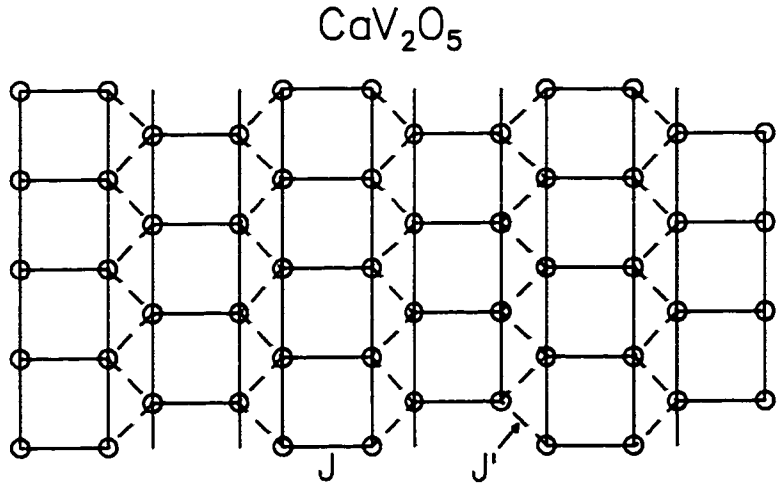

Figure 3.11: Structure of CaV_2O_5 viewed along the c-axis. The solid lines are the ladder structures formed with a corner-sharing interaction J and the dashed lines are the zig-zag chain structures with a edge-sharing interaction J'.

relaxation rates in both ZF and longitudinal field $H_L = 1$ kG, respectively, of polycrystalline CaV_2O_5. Filled symbols are fits to a single exponential relaxation function in the ZF spectra while open symbols are the relaxation rate of the longer-lived tail component in a two-component fit in the longitudinal field (LF) spectra. The relaxation rate in the LF reaches a maximum value at $T = 50$ K. This indicates spin freezing below 50 K and the possibility that a substantial fraction of the vanadium magnetic moment is not in a spin-singlet ground state [39].

We have also performed μSR measurements in all known two-leg ladder compounds and found an absence of spin freezing in $SrCu_2O_3$ down to $T = 100$ mK [44], an antiferromagnetic ground state with clear muon spin precession in $LaCuO_{2.5}$, and dynamic spin fluctuations in MgV_2O_5 (which we

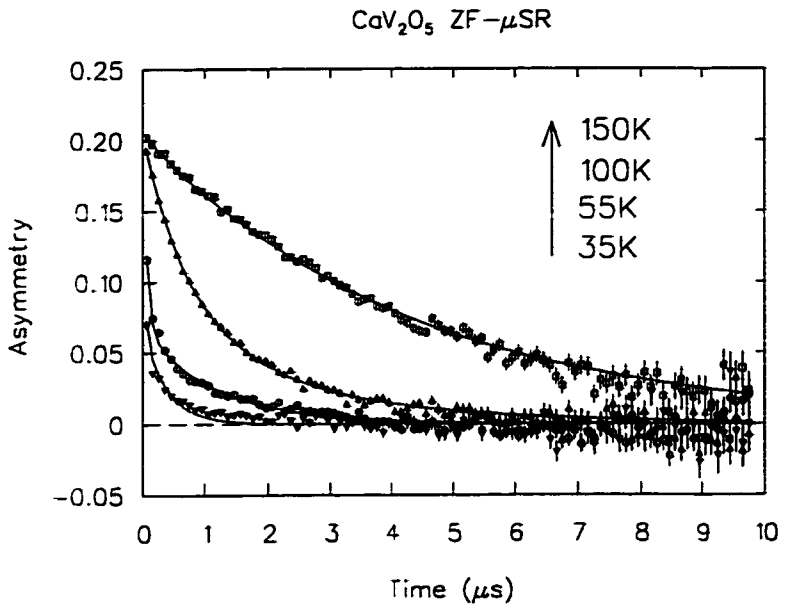

Figure 3.12: Zero-field μSR spectra of polycrystalline CaV_2O_5.

discuss next) down to $T = 2.5$ K. The variation in ground state of these compounds is presumably related to the difference in their inter-ladder interactions.

Two-Leg Ladder MgV_2O_5

MgV_2O_5 has the identical two-leg ladder structure as CaV_2O_5. Nevertheless, we observed dynamic spin fluctuations in polycrystalline MgV_2O_5down to $T = 2.5$ K in our μSR measurements.

We fit the μSR spectra in the longitudinal field $H_L = 100$ G (Fig. 3.13) to the phenomenological function: $\mathcal{A}(t) = A\exp[-(\lambda)^{\beta}]$, and show the temperature dependence of the relaxation rate λ in Fig. 3.14. λ increases monotonically with decreasing temperature.

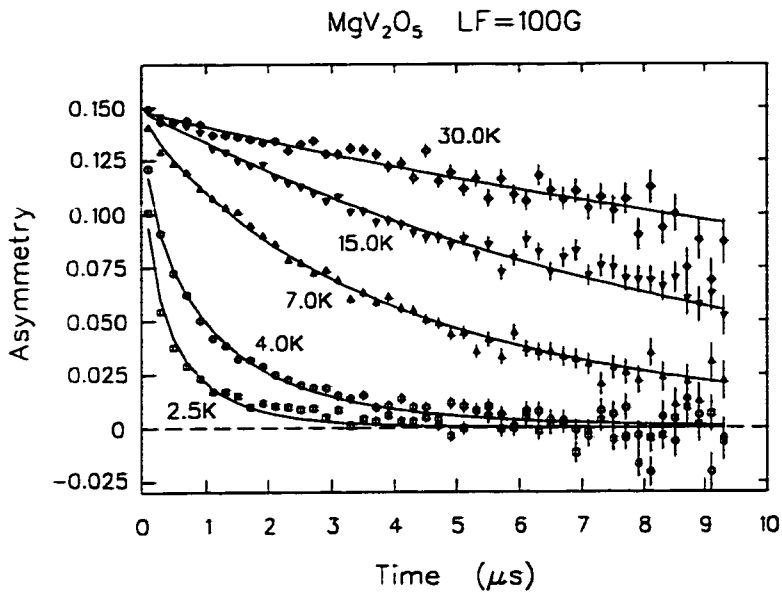

Figure 3.13: The μSR spectra of polycrystalline MgV_2O_5 in the longitudinal field H_L = 100 G.

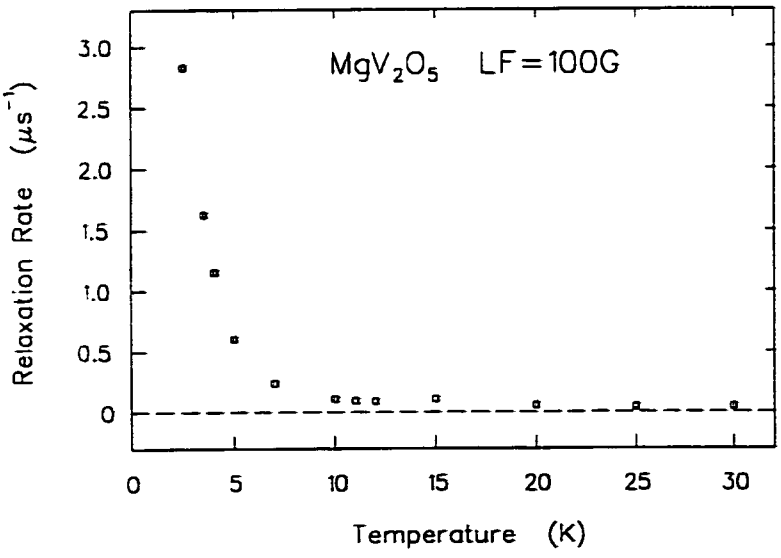

Figure 3.14: Temperature dependence of the relaxation rate λ in the μSR spectra of polycrystalline MgV_2O_5 in the longitudinal field H_L = 100 G.

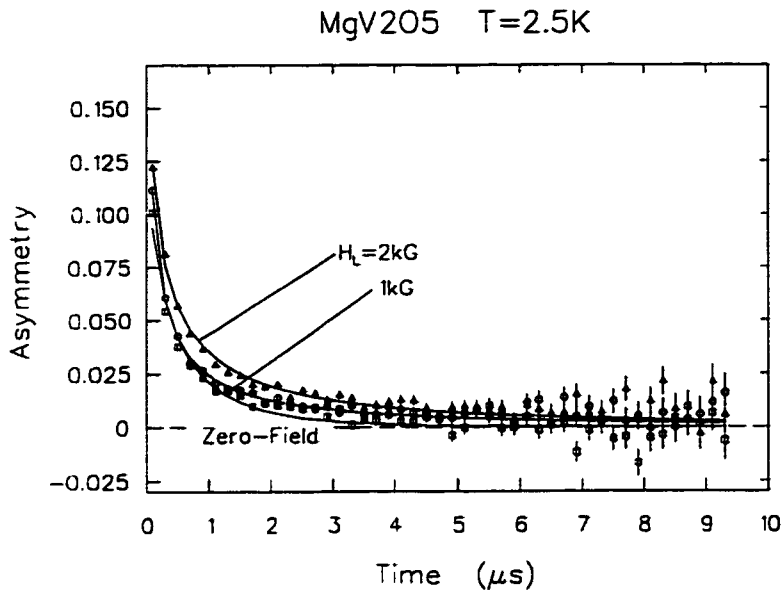

Figure 3.15: The μSR spectra of polycrystalline MgV_2O_5 at $T = 2.5$ K, in the longitudinal fields $H_L = 100$ G, 1 kG, and 2 kG.

In Fig. 3.15, we show the spectra at $T = 2.5$ K in several longitudinal fields $H_L = 100$ G, 1 kG, and 2 kG. The relaxation does not decouple in the high field $H_L = 2$ kG, and thus we confirm the presence of dynamic spin fluctuations down to 2.5 K. The μ SR results of MgV_2O_5 are similar to those of two-leg ladder cuprate $SrCu_2O_3$, in which we have also found an existence of dynamic spin fluctuations down to $T = 200$ mK [44].

We have also measured the susceptibility of MgV_2O_5 using a SQUID DC magnetometer, and confirmed the existence of a spin gap $\Delta \sim 120$ K. Since the apparent spin gap in MgV_2O_5 is smaller than that inferred in CaV_2O_5 ($\Delta \sim 500$ K), we might expect MgV_2O_5 will also order magnetically with the ordering temperature which is much reduced from the ordering temperature of 50 K in CaV_2O_5.

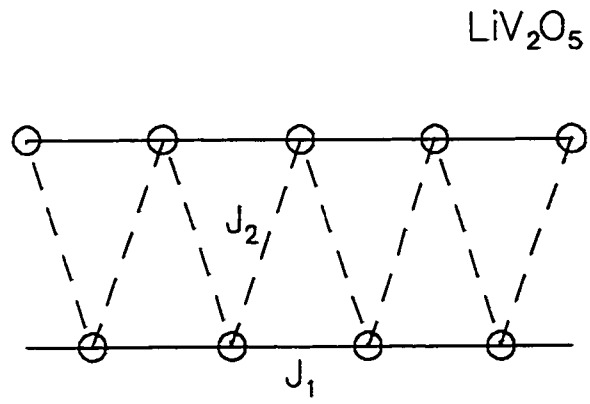

Figure 3.16: The zig-zag spin ladder system in LiV_2O_5.

Zig-Zag Chain LiV_2O_5

Corner-sharing $V^{4+}O_5$ form an infinite linear chain in LiV_2O_5. In addition, two adjacent linear chains are paired by edge-sharing to form a zig-zag chain. Thus, LiV_2O_5 forms a quasi-1-D spin 1/2 system consisting of linear chains with a first-neighbor coupling J_1 and a frustrating second-neighbor coupling J_2 (Fig. 3.16). The relative sizes of J_1 and J_2 are not yet known in this system.

The ground state of zig-zag spin chains has been theoretically predicted to be a spin-singlet state induced by dimerization (possibly without lattice distortion) along with the formation of a spin gap [58]. The singlet ground state is expected to appear in a wide range of coupling constant ratio J_1/J_2, and the size of gap is estimated as $\Delta \propto \exp[-const. \times (J_1/J_2)]$. Thus, the gap size is exponentially diminishing when $J_1/J_2 \ll 1$ (i.e. the purely 1-D situation).

The susceptibility data of LiV_2O_5 are consistent with a $S = 1/2$ 1-D

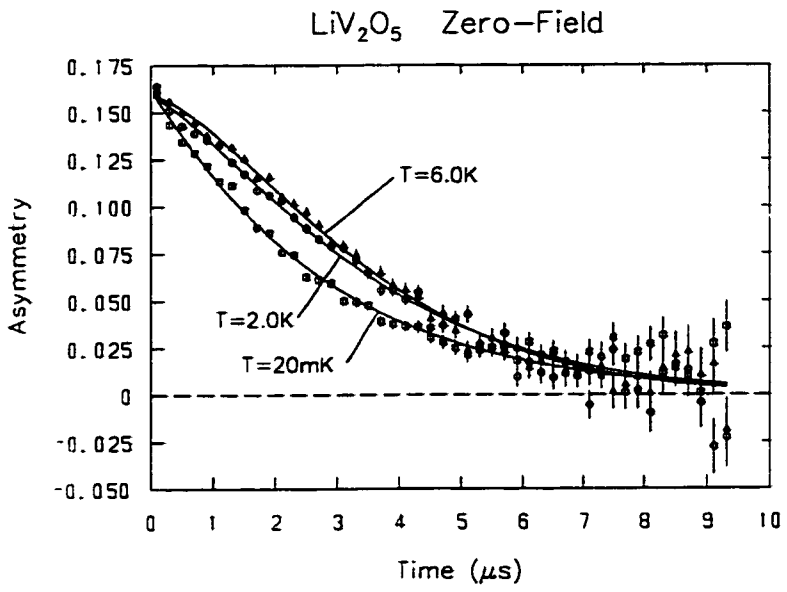

Figure 3.17: Zero-field μSR spectra of polycrystalline LiV_2O_5 at $T = 20$ mK, 2.0 K and 6.0 K.

Heisenberg antiferromagnetic model and the coupling constant was estimated to be $|J|/k_B = 154$ K [59]. Saturation to a finite susceptibility at the lowest temperature might indicate the absence of a spin-singlet ground state. Spin fluctuations were also studied by ^{7}Li-NMR [60]. The T_1-relaxation rate exhibit a minimum at $T \sim 30$ K. Furthermore, the logarithmic increase of $1/T_1$ was observed at low temperature as predicted in the recent theory of an isotropic Heisenberg linear chain [61].

Figure 3.17 shows zero-field μSR spectra measured in polycrystalline LiV_2O_5 at $T = 20$ mK, 2.0 K and 6.0 K. The faster relaxation as $T \to 0$ may be caused by spin slowing down towards magnetic order. The zero-field spectra are fit to: $\mathcal{A}(t) = A\exp[-(\lambda t)^\beta)]$, and Fig. 3.18 shows temperature dependence of the relaxation rate λ. λ is increased below $T \sim 2$ K. There is

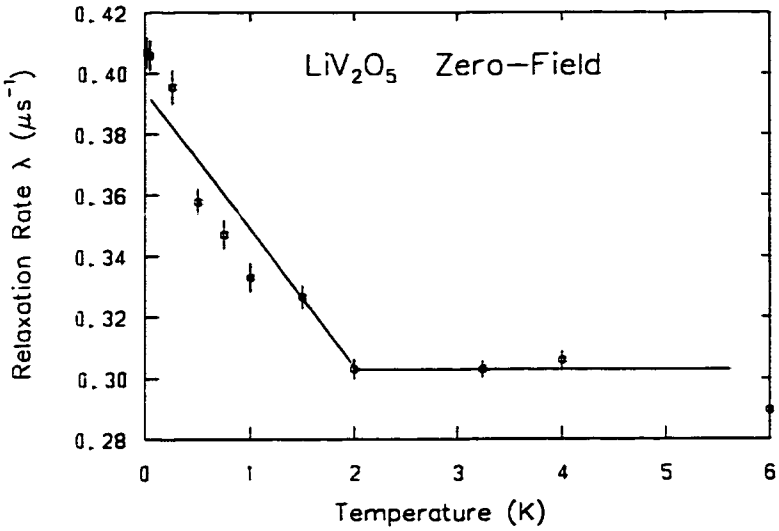

Figure 3.18: Temperature dependence of the relaxation rate λ in the zero-filed spectra of polycrystalline LiV_2O_5 at $T = 50$ mK.

in fact longitudinal field dependence in the spectra at $T = 50$ mK (Fig. 3.19. implying some magnetic order might occur at low temperature. The internal field estimated from this decoupling is ~ 20 G. This result could be compared to observed spin freezing at $T = 2$ K in $SrCuO_2$, which implies a larger J_1/J_2 ratio in that material than in LiV_2O_5.

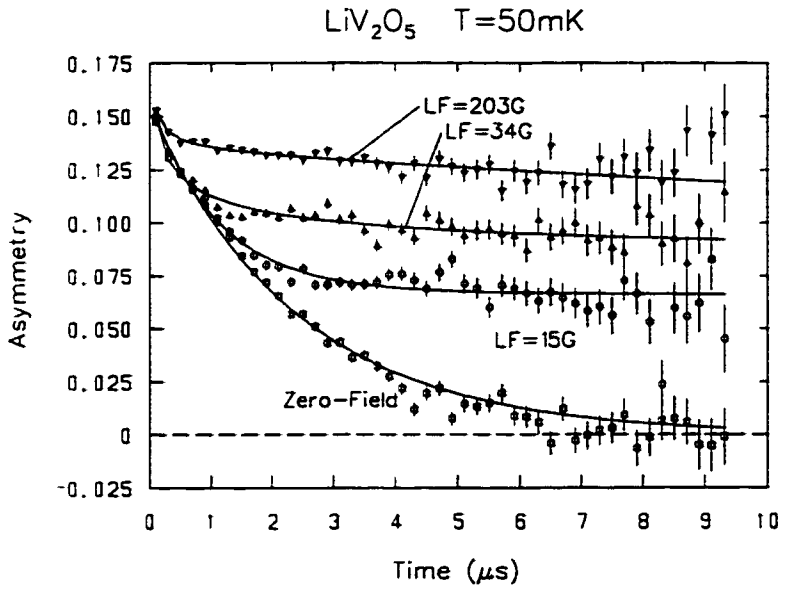

Figure 3.19: Longitudinal-field μSR spectra of polycrystalline LiV_2O_5 at T = 50 mK.

Chapter 4

Static Spin Freezing in Spin-Ring System Cu_3WO_6

In this chapter, we present muon spin relaxation (μSR) measurements of polycrystalline $Cu_{3-x}Zn_xWO_6$. We have observed static spin freezing at $T = 7.0$ K in pure Cu_3WO_6 with a small average ordered moment. In Zn-doped $Cu_{3-x}Zn_xWO_6$ with $x = 0.01$, 0.05, and 0.10, however, no spin freezing is observed down to $T = 2.20$ K, 0.10 K, and 0.10 K, respectively. We discuss similarities between the μSR results of $Cu_{3-x}Zn_xWO_6$ and those of a charge-ordered system $Na_xV_2O_5$ and other widely accepted spin-gap systems. A few possible interpretations of the observed spin freezing will also be provided.

4.1 Singlet Ground State of Six-Spin-Ring in Cu_3WO_6

Cu_3WO_6 is a spin-gap system, which contains 1-D magnetic rings consisting of six $S = 1/2$ nearest-neighbor spins coupled antiferromagnetically. The crystal structure of Cu_3WO_6 has a cubic unit cell with space group $Pa\bar{3}$-T_h^6 and lattice constant $a = 9.79$ Å [62]. It consists of distorted WO_6 octahedra

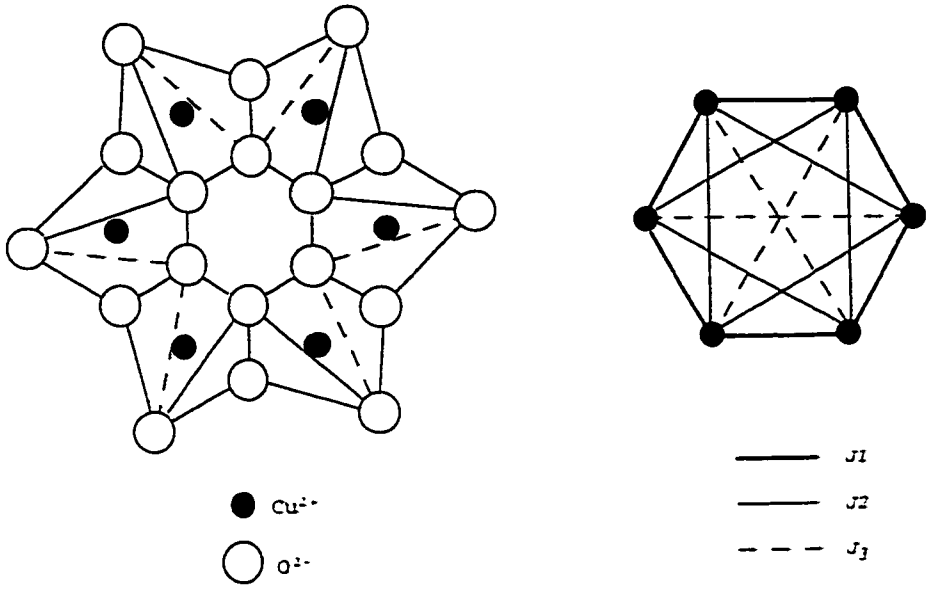

Figure 4.1: (*left*) A six-spin ring in Cu_3WO_6, formed by CuO_5 bipyramids. Solid and Open circles represent Cu^{2+} and O^{2-} ions, respectively. Cu^{2+} ions in the ring are coupled by the nearest neighbor interactions. (*right*) The first (J_1), the second (J_2), and the third (J_3) nearest-neighbor interactions within the ring.

and CuO_5 triangular bipyramids, in which only a Cu^{2+} ion (located inside the bipyramid) has a localized spin ($S = 1/2$). Each CuO_5 bipyramid shares an edge with two other bipyramids and a corner with four other bipyramids. Six adjacent edge-sharing bipyramids then form a ring (Fig. 4.1). The distance between two Cu^{2+} ions located in two edge-sharing bipyramids is 2.99 Å, while the distance in two corner-sharing bipyramids is 3.22 Å or 3.53 Å. Thus, six $S = 1/2$ Cu^{2+} spins in the bipyramid are coupled with the nearest-neighbor interaction to form a six-spin ring. These six-spin rings, however, are not isolated perfectly since Cu^{2+} ions in the ring are also coupled with other Cu^{2+} ions by the corner-sharing coupling.

Susceptibility measurement of polycrystalline Cu_3WO_6 indicated the ex-

istence of a spin-singlet ground state with a gap $\Delta = 110$ K [63]. At high temperatures the experimental value of the susceptibility is much lower than a theoretical value [64]: about 2/3 lower around their maxima. The lowerness of the susceptibility could be attributed to a possible resonating-valence bond state.

Two peaks at 11 meV and 14 meV were observed in constant-Q energy spectra of inelastic neutron scattering measurements [65], and were consistent with theoretical calculations of the singlet-triplet excitations with $J_2/J_1 = 0.64$ and $J_3/J_1 = 0.51$, where J_1, J_2, and J_3 are the first, the second, and the third nearest-neighbor antiferromagnetic exchange interactions respectively, within the ring (Fig. 4.1). However, the observed susceptibility curves could not be reproduced assuming these values of the superexchange couplings, probably because of the existence of inter-ring interactions.

4.2 Sample Characterizations

Using a SQUID magnetometer, we measured the magnetic susceptibility of the specimens used in the present μSR study. Figure 4.2 shows the results obtained in applied external field of 50 G. The susceptibility χ(T) of both the undoped and the doped specimens indicate the Curie (1/T) type increase at low temperatures, which corresponds to the existence of free spins. $\chi(T)$ at low temperatures are fit with:

$$\chi(T) = \frac{C}{T-\theta} + A\exp\left(-\frac{\Delta}{T}\right) + K, \tag{4.1}$$

where the first term represents the Curie-Weiss behavior due to free spins, the second term represents the gap excitation, and the third term is a constant.

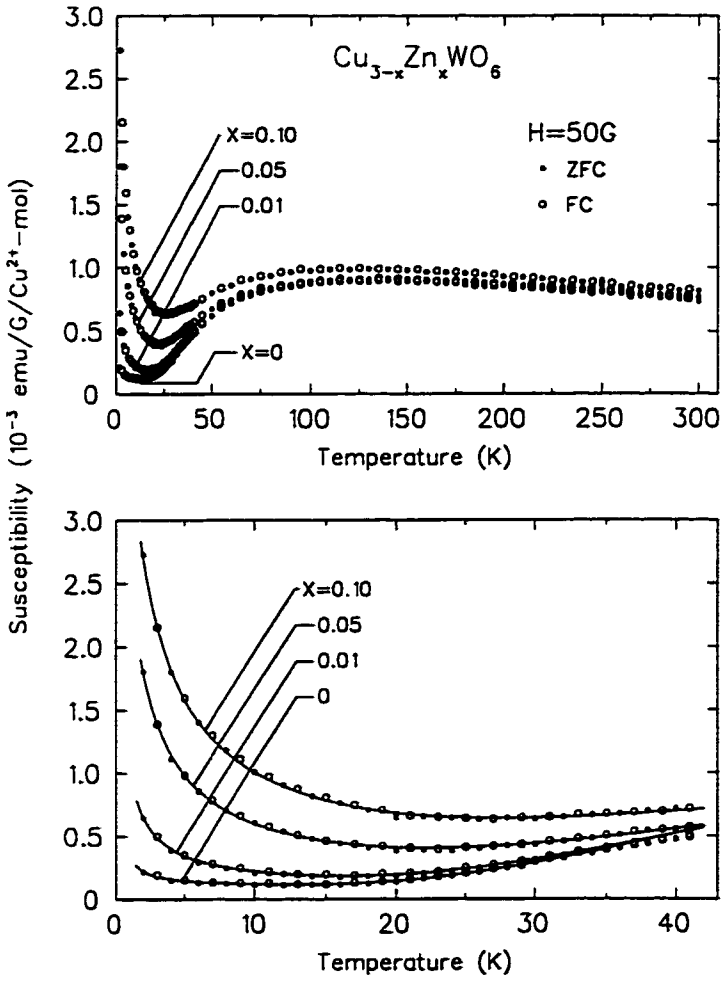

Figure 4.2: Susceptibility of $Cu_{3-x}Zn_xWO_6$. Solid lines represent Eq. 4.1.

Table 4.1: List of parameters obtained from the best fit of the susceptibility of polycrystalline $Cu_{3-x}Zn_xWO_6$ (Fig. 4.2) to Eq. 4.1 at low temperatures. Units of C, A, and K are (emu/Gauss/Cu^{2+}-mol).

x	$C \times 10^{-4}$	θ(K)	$A \times 10^{-3}$	Δ(K)	$K \times 10^{-5}$	%-impurity	$x/3.00$ (%)
0	2.49	0	4.70	96.5	9.52	0.0663	0
0.01	14.0	-0.51	4.17	93.9	8.81	0.373	0.33
0.05	52.2	-1.14	2.67	87.3	12.9	1.39	1.66
0.10	88.3	-1.61	1.91	82.6	24.4	2.35	3.33

Table 4.1 is the list of parameters obtained from the best fit. The numbers of impurities calculated form the Curie term are also included in Table 4.1 and indicated as %-impurity. These %-impurities for the Zn-doped specimen fairly agree with desired doping concentrations, indicated as $x/3.00$ in Table 4.1. Note that the Curie-Weiss form is used, rather than the Curie form (C/T), to obtain better results in the fitting, but the magnitudes of θ remain smaller than the lowest temperature limit of 2 K in the measurements.

4.3 Static Spin Freezing at 7.0 K

Figure 4.3(a) shows time spectra of the muon spin polarization in polycrystalline Cu_3WO_6 in zero external field (ZF). Below $T = 7.0$ K, fast reduction of muon spin polarization (about 0.061 reduction of asymmetry), followed by slow relaxation (0.074 of asymmetry), is observed. The fast relaxation implies the existence of large local field caused by static electron spins. The relaxation becomes slower with increasing temperatures. Above 7.0 K, the fast static relaxation is no longer observed, and thus the system is

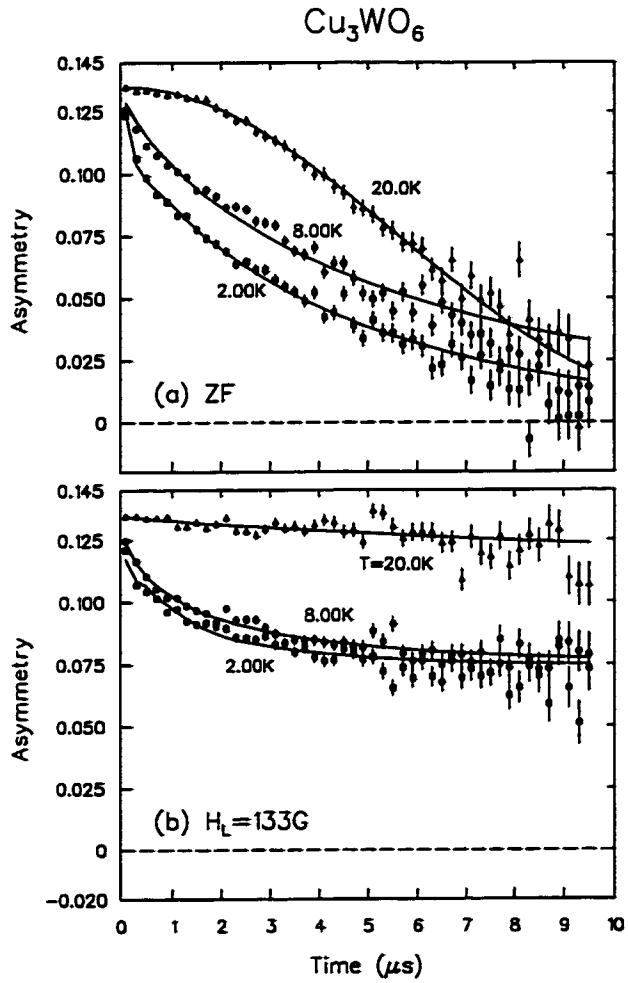

Figure 4.3: μSR spectra of polycrystalline Cu_3WO_6; (a) in zero external field and (b) in the longitudinal field H_L = 133 G. Solid lines are guides to the eye.

clearly in the paramagnetic state. Above 20.0 K, only slow relaxation caused by static nuclear moments remains.

In the moderately high longitudinal field of $H_L = 133$ G, the slow relaxation, as well as the relaxation due to nuclear dipoles, is thoroughly suppressed [Fig. 4.3(b)]. This implies the static nature of the slow relaxation. The existence of two static relaxations implies two magnetically inequivalent muon environments, one with large characteristic local field and another with much smaller field. However, the static relaxation caused by the small local field is so slow that it is hard to determine the lineshape of the spectra and consequently the origin of the relaxation. Therefore, in the following discussion, we limit our discussion to the fast relaxation of the signal.

In Fig. 4.4(a), we show spectra in $H_L = 133$ G at early times. The local field causing the fast muon spin relaxation is decoupled by longitudinal fields (LF) of 133 G $< H_L <$ 1 kG [Fig. 4.4(b)], confirming the static nature of the observed fast relaxation. The magnitude of the internal field estimated from this decoupling is $H_{int} \lesssim 100$ G. The ordered Cu^{2+} moment is then estimated as roughly $\sim 0.1\mu_B$. There is, however, no sign of coherent oscillation of the muon spin polarization, indicating the broadness the distribution of the local field, and therefore the randomness of the directions of frozen electron spins. The Curie term in the susceptibility of our specimen corresponds to 0.08 % of free spin-1/2 moments, which could create only $\sim$ 0.6 G of internal field. The observed static fields of $H_{int} \lesssim 100$ G thus cannot be ascribed to impurities in the specimen. The slow relaxation present even in LF is caused by dynamic fluctuations of the electron moments, and these fluctuations are persisting even at $\sim$ 2.0 K.

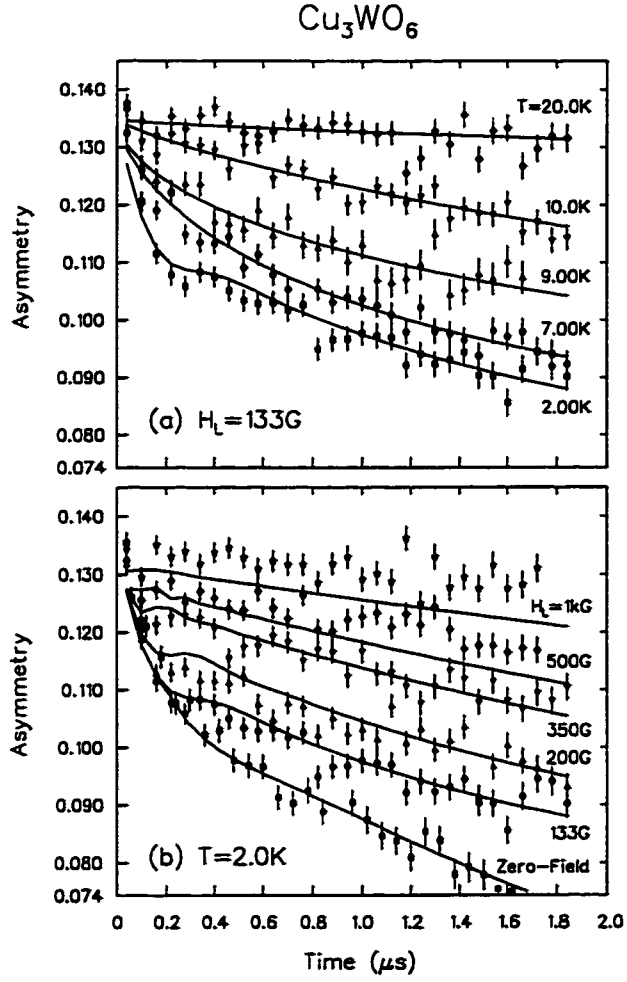

Figure 4.4: (a) μSR spectra of polycrystalline Cu_3WO_6 in the longitudinal field H_L = 133 G at early time. Solid lines represent the best fit to Eq. 4.2 below T = 7.0 K and Eq. 4.4 above 7.0 K. (b) LF μSR spectra of polycrystalline Cu_3WO_6 at T = 2.0 K. Solid lines correspond to Eq. 4.2, with fixed a = 2.85 μs^{-1} and ν = 2.25 μs^{-1} obtained from the best fit in the spectra at T = 2.0 K. The spectra are decoupled approximately following the theoretical lineshapes.

The spectra in H_L = 133 G below T_f =7.0 K are well fitted with the function:

$$A(t) = A_1 G^L(a, \nu, t; H_L) + A_2, \tag{4.2}$$

where the first term represents the fast static relaxation and the second term the decoupled slow relaxation component. $A_1 = 0.061$ is the observed initial asymmetry of the fast relaxation component and A_2 =0.074, while $G^L(a, \nu, t; H_L)$ is the LF relaxation function for the Lorentzian field distribution with fluctuating moments. a is the static relaxation rate (or a half-width half-maximum of the Lorentzian distribution), and ν is the fluctuation rate. For ZF (H_L = 0 G) and no fluctuation ($\nu = 0\ \mu s^{-1}$), $G^L(a, \nu, t; H_L)$ reduces to Eq. 2.19. In the long time limit, any function for coexisting static and dynamic relaxation has the asymptotic form $G(\lambda, t) \sim \frac{1}{3}\exp[-(\lambda t)^\beta]$, where λ is the dynamic relaxation rate. The stretching power β has a value $\beta = 1/2$ for the case of spatially dilute spin systems (and $\beta = 1$ for dense spin systems) with a single dynamic fluctuation rate. β often takes different values in spin glass systems, which often possess a distribution of dynamic fluctuation rates. To obtain the dynamic relaxation, we therefore fit the spectra for $t >$ 0.5 μs with the function:

$$A(t) = A_1' \exp[-(\lambda t)^\beta] + A_2. \tag{4.3}$$

A_1' is left as a free parameter and remains around $\sim$ 0.5, and β is allowed to vary in the range $\beta < 1.0$. In the paramagnetic phase, the relaxation is entirely due to the dynamic process of the electron spins. Above T_f the LF spectra in H_L = 133 G are thus analyzed with:

$$A(t) = A_1 \exp[-(\lambda t)^\beta] + A_2, \tag{4.4}$$

for the entire time range.

In high longitudinal field $H_L \geq 500$ G, the fast static relaxation at low temperatures is well suppressed and the persisting slow relaxation is due only to the dynamic processes of the electron spins. Thus, the spectra in $H_L = 500$ G are analysed with Eq. 4.4 for the entire temperature range.

Temperature dependences of the static relaxation rate a, the dynamic relaxation rate λ, and the stretching exponent β are given in Fig. 4.5(a), (b), and (c), respectively. The sharp reduction of the static relaxation rate a, the divergence of the dynamic relaxation rate λ, and the decrease of the stretching exponent β are characteristic features of the random spin freezing systems around the freezing temperature. The static relaxation rate a gives an internal field at which the probability distribution of the field magnitude $P(H) = [\gamma_\mu^3/\pi^2] \times [a/(a^2 + \gamma_\mu^2 H^2)]^2 \times 4\pi H^2$ takes its maximum value, and $a = 2.85\ \mu s^{-1}$ at $T = 2.0$ K corresponds to the field of $H_{max} = a/\gamma_\mu = 34.0$ G. We can estimate the fluctuation rate ν of the fluctuating moments in the paramagnetic phase $T > T_f$ using $\lambda = 1/T_1 \sim a^2/\nu$. Since the stretched exponential function with $\beta \ll 1.0$ has a very sharp reduction at early times, the relaxation rate resulting from the stretched exponential fit with the low β values tend to underestimate an average depolarization rate. To compensate this effect, we calculate $\lambda^* = \ln(2)/[\ln(2)]^{1/\beta} \times \lambda$. Figure 4.6 shows the the average fluctuation rate $\nu^* \sim a^2/\lambda^*$. Comparing with activation behavior:

$$\nu^* \propto \exp\left(-\frac{E_g}{k_B T}\right), \tag{4.5}$$

we obtain a gap energy $E_g = 44.6$ K, which is roughly half of the spin-gap energy $E_g \sim 110$ K obtained in the susceptibility [63] and neutron measurements [65], but much larger than the freezing temperature $T_f = 7.0$ K.

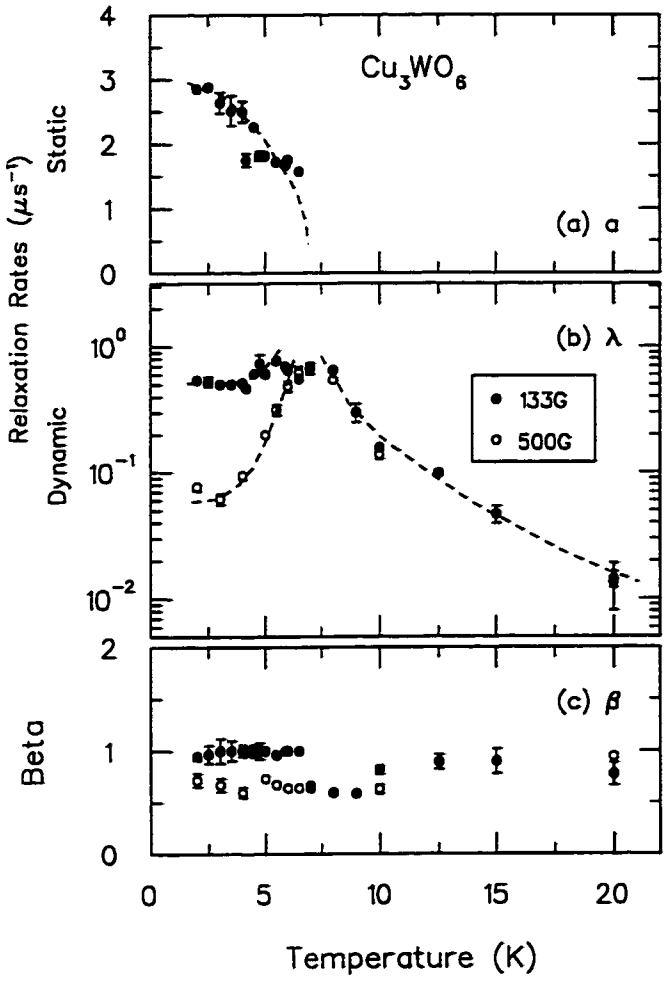

Figure 4.5: Temperature dependences of (a) the static relaxation rate a, (b) the dynamic relaxation rate λ, and (c) the stretching exponent β, defined in Eqs. 4.2 $\sim$ 4.4. Broken lines are guides to the eye.

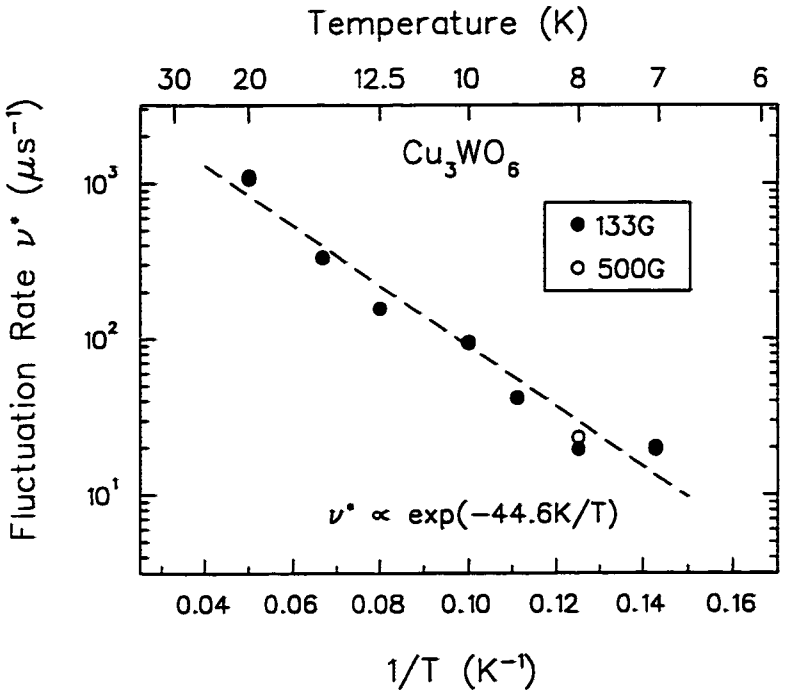

Figure 4.6: Temperature dependence of the average fluctuation rate ν^* of the the fluctuating local fields in polycrystalline Cu_3WO_6. The broken line corresponds to the thermal activation behavior (Eq. 4.5).

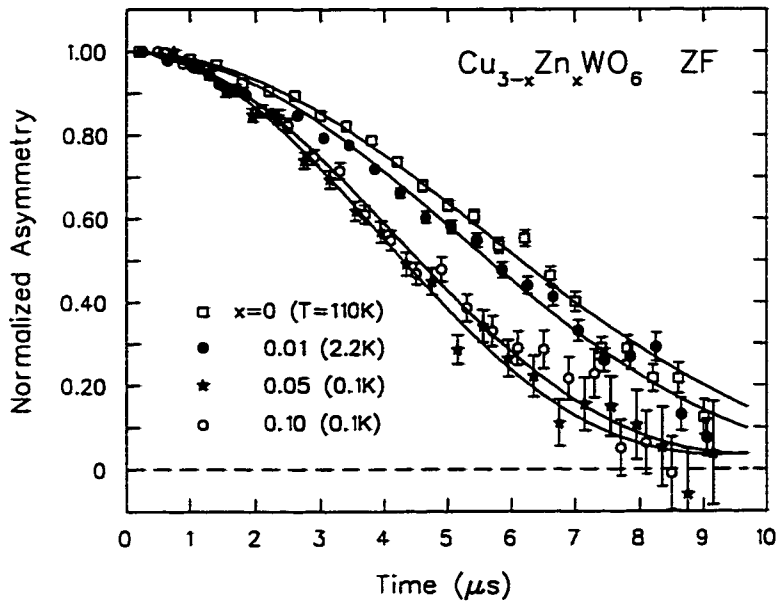

Figure 4.7: ZF-μSR spectra of $Cu_{3-x}Zn_xWO_6$ at low temperatures. The ZF spectra of pure Cu_3WO_6 at $T = 110$ K is also included to show the relaxation of nuclear fields.

4.4 Suppression of Spin Freezing by Magnetic Dilutions

Cu_3WO_6 can be magnetically diluted by substituting nonmagnetic Zn^{2+} (spin-0) for magnetic Cu^{2+} (spin-1/2) ions. With increasing Zn-doping, a sharp reduction of the susceptibility towards $T \rightarrow 0$ is suppressed [66] (Fig. 4.2), indicating the suppression of a spin-gap formation.

Figure 4.7 shows ZF-μSR spectra of $Cu_{3-x}Zn_xWO_6$ with $x = 0.01$, 0.05, and 0.10 at low temperatures. The fast relaxation caused by nearly static electron spins observed in pure Cu_3WO_6 no longer exists, and only a slow relaxation due to nuclear dipoles are observed. A small amount of (Cu,

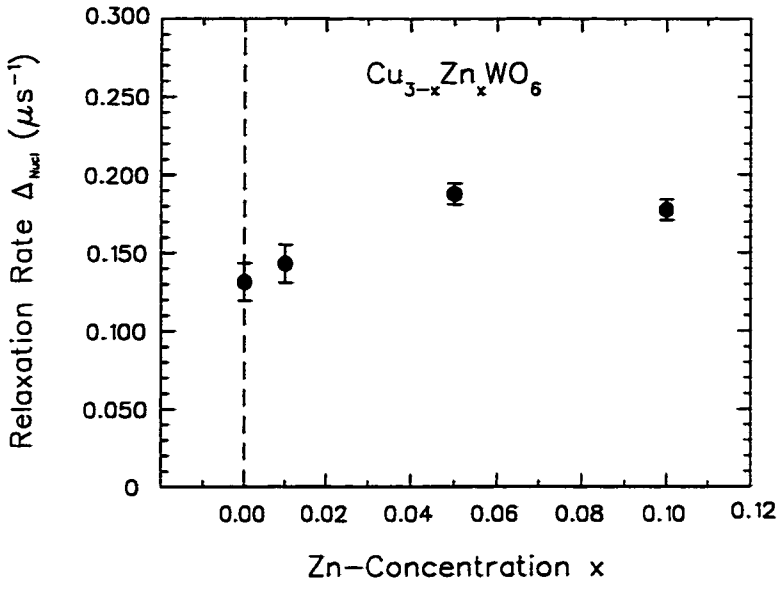

Figure 4.8: Zn-concentration x versus relaxation rate Δ_{Nucl} defined in Eq. 4.6.

Zn) substitution is thus enough to enhance the fluctuation of electron spins drastically and eliminate the quasi-static component.

The spectra are consistent with $A(t) = AG^G(\Delta_{Nucl}, t)$, where

$$G^G(\Delta, t) = \frac{1}{3} + \frac{2}{3}(1 - \Delta^2 t^2)e^{-\frac{\Delta^2 t^2}{2}} \tag{4.6}$$

is the Gaussian Kubo-Toyabe function, and Δ_{Nucl} is a static relaxation rate due to random local fields created by nuclear dipoles. Figure 4.8 shows the x dependence of the relaxation rate Δ_{Nucl}. The relaxation rate remains small at very low temperature, and thus there is no sign of critical slowing down nor phase transition of electron spins. We note that the relaxation rate is slightly increased with increasing Zn-concentration x. We would rather expect the reduction of the relaxation rate by Zn-substitution because Zn has no nuclear

spin ($I = 0$) while Cu has $I = 3/2$ and because Zn^{2+} has larger ionic radius than Cu^{2+}. The origin of this effect is unclear at this moment.

4.5 Discussion

Non-magnetic ground states of quasi-1-D systems, such as $CuGeO_3$ [4] and $SrCu_2O_3$ [5], are usually altered to antiferromagnetic order by slight magnetic dilution. Recently, hole-induced long-range order was also discovered in a new Haldane system $PbNi_2V_2O_8$ [67]. Static spin freezing in a spin-ring system Cu_3WO_6, and its suppression by hole doping is quite peculiar compared to the above examples of 1-D spin systems. On the other hand, static spin freezing behavior has been detected by μSR in other widely accepted spin gap systems, such as a plaquette spin system CaV_4O_9 [39] and a zig-zag chain system $KCuCl_3$ [40]. Remarkable similarities to the present case are found in the μSR results of the charge-ordered system $Na_xV_2O_5$ (Chapter 3) [26, 27]. Pure NaV_2O_5 has a spin-ladder structure, and is thought to undergo a charge-order transition at $T_c = 35$ K; from a state of a mixed valence of Vanadium ions $V^{4.5+}$ above T_c to a localization of d-electrons to form a spin-singlet below T_c. A gap energy in susceptibility is suppressed in a charge-doped system ($x < 1$) [42]. Static spin freezing at 11 K has been detected by μSR in the pure system ($x = 1$) while the freezing is suppressed in the charge-doped system ($x < 1$) [26]. The magnetic behavior of pure and charge-doped NaV_2O_5 detected by μSR is very similar to that of Cu_3WO_6.

A good agreement between the observed energy gaps in neutron scattering measurements and the theoretical singlet-triplet excitation calculation strongly supports a singlet ground state of the spin-rings in Cu_3WO_6. As

mentioned in Sec. 4.3, however, the gap energy $E_g \sim 44.6$ K is much larger than the freezing temperature $T_f = 7.0$ K, which indicates the existence of two distinct electron systems. We propose a model where part of the spin system forms a spin-singlet state while the remainder undergo spin freezing below T_f. As Zn^{2+} are doped, some holes cut the spin-ring and leave it as a finite spin chain. Spins within a finite chain are generally expected to fluctuate without any spatial correlations to each other, leading to a disappearance of the gap energy. These fluctuations then induce fluctuations of the spins corresponding to the freezing spins in the undoped compound. The magnetically inequivalent muon environments observed in the ZF spectra below 7.0 K could be attributed to two kinds of the spin states at low temperature proposed above. If we assume the slow relaxation is due to volume occupied by spin singlets and the fast relaxation by freezing spins, then about 40 % of the spins would undergo static spin freezing below 7.0 K.

The possibility of a muon-induced effect was proposed to explain the spin glass like behavior in $KCuCl_3$ [68]. In that study it was postulated that the presence of the μ^+ could destroy singlet pairs and those liberated spins develop a quasi static behavior in part of volume, while relatively slow fluctuations persist in the remaining volume. Similar muon-induced static freezing is also proposed for organic spin-Peierls $MEM(TCNQ)_2$ [69]. These muon effects is analogous to an effect of (Ge, Si) substitution in $CuGeO_3$ [70, 71]. The presence of a positive charge (μ^+) could cause local strain to perturb the lattice, prevent spin-singlet formations, and induce static freezing of spins around μ^+. At present, however, these muon-induced effects are neither confirmed nor excluded.

One should also be aware of the time scale to which the measurement refers. Dynamic spin fluctuations can be detected μSR in a time window of fluctuation rates ν ranging between $10^7 \sim 10^{12}$ s^{-1}. However, if a correlation time is much larger than the muon life time $\tau_\mu = 2.2$ μs, then muons would see "virtually static" electron spins. Hysteresis in the susceptibility in FC/ZFC process, a characteristic feature of spin glass systems, is in fact absent (Fig. 4.2). Further study is required using complimentary magnetic probes having different time scales, like AC susceptibility and NMR, for better understanding of the magnetic behavior of Cu_3WO_6.

Chapter 5

Conclusions

Magnetic properties of charge-ordered system $Na_xV_2O_5$ and spin-ring system $Cu_{3-x}Zn_xWO_6$ were studied utilizing the muon spin relaxation (μSR) technique.

Static spin freezing at $T \sim 11$ K was detected in NaV_2O_5, which is widely considered to have a spin-singlet state below 35 K. This spin freezing has disappeared in charge-doped Na deficit samples $Na_xV_2O_5$ with $x = 0.99$ and 0.90, in which spin gap formation is also suppressed. To ascribe observed internal magnetic field, more than 10 % of the magnetic V moments should undergo static freezing.

Static spin freezing is also observed below $T = 7.0$ K in pure Cu_3WO_6 with a very small average ordered moments of $\sim 0.1\mu_B$. Zn-doped $Cu_{3-x}Zn_xWO_6$ with $x = 0.01$, 0.05, and 0.10, however, exhibit no signatures of spin freezing down to $T = 2.20$ K, 0.1 K, and 0.1 K, respectively. The μSR results of $Cu_{3-x}Zn_xWO_6$ are similar to those of a charge-ordered system $Na_xV_2O_5$.

In summary, this thesis presents two new and unique results on quasi-one-dimensional spin systems characterized by the formation of a spin gap. Firstly, static nature of a substantial fraction of the electron spins has been

Table 5.1: Summary of the μSR results in widely accepted spin gap systems.

Compound	Susceptibility/NMR/Neutron	μSR
NaV_2O_5	Spin Gap $\Delta = 98$ K (NMR) $\Delta = 10$ meV (Neutron)	Static Spin Freezing $T_f = 11$ K
CaV_2O_5	Spin Gap (Two-Leg Ladder) $\Delta = 616$ K (NMR)	Static Spin Freezing $T_f = 50$ K
MgV_2O_5	Spin Gap $\Delta \sim 120$ K (Susceptibility)	Dynamic Spin Fluctuations down to 2.5 K
LiV_2O_5	Dynamic Spin Fluctuations	Critical Slowing Down (?)
CaV_4O_9	Spin Gap $\Delta \sim 100$ K	Static Spin Freezing $T_f = 12$ K
Cu_3WO_6	Spin Gap $\Delta \sim 110$ K	Static Spin Freezing $T_f = 7$ K

revealed by muon spin relaxation for the first time in NaV_2O_5 and Cu_3WO_6, which have been widely considered as a spin gap system based on previous susceptibility, NMR, and/or neutron scattering studies (Table 5.1). Secondly, unusual doping effects are observed in these materials, namely the disappearance of staticness in charge-doped $Na_xV_2O_5$ and magnetically diluted $Cu_{3-x}Zn_xWO_6$, which are quite peculiar compared to the cases of ordinary quasi-1-D spin systems (Table 5.2). These results should stimulate the discussion on physical properties of systems of this type and hopefully induce additional measurements, especially nuclear quadrupole resonance measurements in zero-field and nuclear magnetic resonance measurements in low-field, to confirm observed anomalous magnetic phase transitions and to understand the underlying physical mechanism.

Table 5.2: Unusual doping effects in magnetism of NaV_2O_5 and Cu_3WO_6 detected by μSR as compared to those of other quasi-1-D systems.

Compound	Pure System	Effect of Hole/Charge Dopings
$CuGeO_3$	Singlet Ground State (Spin-Peierls)	Antiferromagnetic LRO (Magnetic Dilutions)
$SrCu_2O_3$	Singlet Ground State (Two-Leg Ladder)	Antiferromagnetic LRO (Magnetic Dilutions)
Y_2BaNiO_5	Singlet Ground State (Haldane)	Static Spin Freezing (Magnetic Dilutions)
NaV_2O_5	Static Spin Freezing	Dynamic Spin Fluctuations (Charge Dopings)
Cu_3WO_6	Static Spin Freezing	Dynamic Spin Fluctuations (Magnetic Dilutions)

Bibliography

[1] M. Hase, I. Terasaki and K. Uchinokura, Phys. Rev. Lett. **70**, 3651 (1993).

[2] M. Azuma, Z. Hiroi, M. Takano, K. Ishida, and Y. Kitaoka, Phys. Rev. Lett. **73**, 3463 (1994).

[3] D.J. Buttrey, J.D. Sullivan and A.L. Rheingold, J. Solid. State Chem. **88**, 291 (1990).

[4] K. Manabe *et al.*, Phys. Rev. B **58**, R575 (1998).

[5] M. Azuma, Y. Fujishiro, M. Takano, M. Nohara, and H. Takagi, Phys. Rev. **B55**, R8658 (1997).

[6] K. Kojima, A. Keren, L.P. Le, G.M. Luke, W.D. Wu, Y.J. Uemure, K. Kiyono, S. Miyasaka, H. Takagi, and S. Uchida, Phys. Rev. Lett. **74**, 3471 (1995).

[7] M. Uehara, T. Nagata, J. Akimitsu, H. Takahashi, N. Mori, and K. Kinoshita, J. Phys. Soc. Japan **65**, 2764 (1996).

[8] J. Des Cloizeaux and J.J. Pearson, Phys. Rev. **128**, 2131 (1962).

[9] J.H. Van Vleck, Phys. Rev. **74**, 1168 (1948).

[10] R. Kubo and T. Toyabe, Magnetic Resonance and Relaxation, 292, North-Holland Publ. Co. (1967).

[11] R.S. Hayano, Y.J. Uemura, J. Imazato, N. Nishida, T. Yamazaki, and R. Kubo, Phys. Rev. B **20**, 850 (1979).

[12] R. Kadono, J. Imazato, T. Matsuzaki, K. Nishiyama, K. Nagamine, and T. Yamazaki, Phys. Rev. B **39**, 23 (1989).

[13] R. Kubo, J. Phys. Soc. Japan **9**, 935 (1954).

[14] M.C. Wang and G.E. Uhlenbeck, Rev.Mod. Phys.**17**, 323 (1945).

[15] Y.J. Uemura, T. Yamazaki, D.R. Harshman, M. Senba, and E.J. Ansaldo, Phys. Rev. B **31**, 546 (1985).

[16] A. Keren, Phys. Rev. B **50**, 10039 (1994).

[17] C.P. Slichter, *Principles of Magnetic Resonance*, Springer-Verlag, Berlin; New York (1990).

[18] C. Kittel and E. Abrahams, Phys. Rev. **90**, 238 (1953).

[19] R.W. Walstedt and L.R. Walker, Phys. Rev. B **9**, 4857 (1974).

[20] R. Kubo, Hyperfine Interact. **8**, 731 (1981).

[21] L.B. Okun, Weak Interactions of Elementary Particles, Pergamon, Oxford (1965).

[22] M. Motokawa, H. Nojiri, K. Nishiyama, K. Nagamine, and T. Yoshida, Physica B **177**, 389 (1992).

[23] K. Nagamine, Y. Miyake, K. Shimomura, P. Birrer, J.P. Marangos, M. Iwasaki, P. Strasser, and T. Kuga, Phys. Rev. Lett. **74**, 4811 (1995).

[24] S. Chu, A.P. Mills Jr., A. Yodh, K. Nagamine, Y. Miyake, and T. Kuga, Phys. Rev. Lett. **60**, 101 (1988).

[25] R.F. Kiefl, J.W. Schneider, H. Keller, W. Kundig, W. Odermatt, B.D. Patterson, K.W. Blazey, T.L. Estle, and S.L. Rudaz, Phys. Rev. B **32**, 530 (1985).

[26] Y. Fudamoto, K.M. Kojima, M.I. Larkin, G.M. Luke, J. Merrin, B. Nachumi, Y.J. Uemura, M. Isobe, and Y. Ueda, Phys. Rev. Lett. **83**, 3301 (1999).

[27] M. Isobe and Y. Ueda, J. Phys. Soc. Japan **65**, 1178 (1996).

[28] Y. Fujii, H. Nakao, T. Yoshihama, M. Nishi, K. Nakajima, K. Kakurai, M. Isobe, Y. Ueda, and H. Sawa, J. Phys. Soc. Japan **66**, 326 (1997).

[29] T. Ohama, H. Yasuoka, M. Isobe, and Y. Ueda, J. Phys. Soc. Japan (in press).

[30] H. Smolinski, C. Gros, W. Weber, U. Peuchert, G. Roth, M. Weiden, and C. Geibel, Phys. Rev. Lett. **80**, 5164 (1998).

[31] H. Seo and H. Fukuyama, J. Phys. Soc. Japan **67**, 2602 (1998).

[32] T. Yoshihama, M. Nishi, K. Nakajima, K. Kakurai, Y. Fujii, M. Isobe, C. Kagami, and Y. Ueda, J. Phys. Soc. Japan **67**, 744 (1998).

[33] C. Gros and R. Valenti, Phys. Rev. Lett. **82**, 976 (1999).

[34] K. Kobayashi, T. Mizokawa, A. Fujimori, M. Isobe, and Y. Ueda, Phys. Rev. Lett. **80**, 3121 (1998).

[35] M. Isobe, C. Kagami and Y. Ueda, J. Cryst. Growth **181**, 314 (1997).

[36] D.R. Noakes and G.M. Kalvius, Phys. Rev. B **56**, 2352 (1997).

[37] M.I. Larkin, Y. Fudamoto, I.M. Gat, A. Kinkhabwala, K.M. Kojima, G.M. Luke, J. Merrin, B. Nachumi, Y.J. Uemura, M. Azuma, and M. Takano, Physica B (in press).

[38] D.R. Noakes, J. Phys. Cond. Matter **11**, 1589 (1999).

[39] G.M. Luke, Y. Fudamoto, M.J.P. Gingras, K.M. Kojima, M. Larkin, J. Merrin, B. Nachumi, and Y.J. Uemura, J. Mag. Mag. Mat. **177-181**, 754 (1998).

[40] W. Higemoto, H. Tanaka, I. Watanabe, and K. Nagamine, Phys. Lett. A **243**, 80 (1998).

[41] I.A. Campbell, A. Amato, F.N. Gygax, D. Herlach, A. Shenck, R. Cywinski, and S.H. Kilcoyne Phys. Rev. Lett. **72**, 1291 (1994).

[42] M. Isobe and Y. Ueda, J. Alloys Comp. **262-263**, 180 (1997).

[43] K.M. Kojima, Y. Fudamoto, M. Larkin, G.M. Luke, J. Merrin, B. Nachumi, Y.J. Uemura, M. Hase, Y. Sasago, K. Uchinokura, Y. Ajiro, A. Revcolevschi, and J.P. Renard, Phys. Rev. Lett. **79**, 503 (1997).

[44] K. Kojima, A. Keren, G.M. Luke, B. Nachumi, W.D. Wu, Y.J. Uemura, M. Azuma, and M. Takano, Phys. Rev. Lett. **74**, 2812 (1995).

[45] A.N. Vasil'ev, V.V. Pryadun, D.I. Khomskii, G. Dhalenne, A. Revcolevschi, M. Isobe, and Y. Ueda, Phys. Rev. Lett. **81**, 1949 (1998).

[46] Y. Ando, J. Takeya, D.L. Sisson, S.G. Doettinger, I. Tanaka, R.S. Feigelson, and A. Kapitulnik, Phys. Rev. B **58**, R2913 (1998).

[47] S. Taniguchi, T. Nishikawa, Y. Yasui, Y. Kobayashi, M. Sato, T. Nishioka, M. Kontani, and K. Sano, J. Phys. Soc. Japan **64**, 2758 (1995).

[48] T. Ohama, H. Yasuoka, M. Isobe, and Y. Ueda, J. Phys. Soc. Japan **66**, 23 (1997).

[49] K. Kodama, H. Harashima, S. Shamoto, S. Taniguchi, M. Sato, K. Kakurai, and M. Nishi, J. Phys. Soc. Japan **65**, 1941 (1996).

[50] K. Kodama, H. Harashima, H. Sasaki, Y. Kobayashi, M. Kasai, S. Taniguchi. Y. Yasui, M. Sato, K. Kakurai, T. Mori, and M. Nishi, J. Phys. Soc. Japan **66**, 793 (1997).

[51] N. Katoh and M. Imada, J. Phys. Soc. Japan **64**, 4105 (1995).

[52] K. Ueda. H. Kontani, M. Sigrist, and P.A. Lee, Phys. Rev. Lett. **76**, 1932 (1996).

[53] M. Troyer. H. Kontani, and K. Ueda, Phys. Rev. Lett. **76**, 3822 (1996).

[54] S. Sachidev and N. Read, Phys. Rev. Lett. **77**, 4800 (1996).

[55] S. Gopalan. T.M. Rice. and M. Sigrist. Phys. Rev. B **49**, 8091 (1994).

[56] T.M. Rice. S. Gopalan. and M. Sigrist, Europhys. Lett. **23**, 445 (1993).

[57] H. Iwase. M. Isobe, Y. Ueda, and H. Yasuoka, J. Phys. Soc. Japan **65**, 2397 (1996).

[58] S.R. White and I. Affleck, Phys. Rev. B **54**, 9862 (1996).

[59] M. Isobe and Y. Ueda, J. Phys. Soc. Japan. **65**, 3142 (1996).

[60] H. Fujiwara. H. Yasuoka, M. Isobe, Y. Ueda, and S. Maekawa, Phys. Rev. B **55**. R11945 (1997).

[61] S. Eggert. I. Affleck, and M. Takahashi, Phys. Rev. Lett. **73**, 332 (1994).

[62] E. Gebert and L. Kihlborg, Acta Chem. Scand. **23**, 221 (1969).

[63] M. Hase and K. Uchinokura, Physica B **215**, 325 (1995).

[64] J.C. Bonner and M.E. Fisher, Phys. Rev. **135**, A640 (1964).

[65] M. Hase. Y. Sasago, K. Uchinokura, K. Hirota, and G Shirane, J. Phys. Soc. Japan **65**. 372 (1996).

[66] N. Koide and K. Manabe, B.S. Thesis, the Univ. of Tokyo (1995).

[67] Y. Uchiyama, Y. Sasago, I. Tsukada, K. Uchinokura, A. Zheludev, T. Hayashi. N. Miura, and P. Bõni, Phys. Rev. Lett. **83**, 632 (1999).

[68] K. Krämer, H.U. Güdel, D. Andreica, F.N. Gygax, M. Pinkpank, A. Schenck, and N. Cavadini, Physica B (in press).

[69] B.W. Lovett, S.J. Blundell, F.L. Pratt, T. Jestädt, W. Hayes, S. Takagi, M. Kurmoo, Physica B (in press).

[70] J.P. Renard, K. Le Dang, P. Vellet, G. Dhalenne, A. Revcolevschi, and L.P. Regnault, Europhys. Lett. **30**, 475 (1995).

[71] H. Fukuyama, T. Tanimoto, and M. Saito, J. Phys. Soc. Japan **65**, 1182 (1996).